Virtual sensing of ocean currents and hydrodynamic drift for underwater gliders via adjoint-based dynamics inversion

Tianshu Wang[†a], Lianbo Wei[†b], Rongshun Juan[a], Yang Li[a], Zezhong Li[c], Jin Chen[c], Yong Zhang[b,*] and Zhongke Gao[a,d,*]

[a] School of Electrical Automation and Information Engineering, Tianjin University, Tianjin 300072, China
[b] the Center for Applied Mathematics and KL-AAGDM, Tianjin University, Tianjin, 300072, China
[c] the School of Mechanical Engineering, Tianjin University, Tianjin 300350, China
[d] Laoshan Laboratory, Qingdao, 266237, China

ARTICLE INFO

Keywords:
Underwater glider
System identification
Adjoint method
Dynamics inversion
Ocean current estimation

ABSTRACT

Underwater gliders, as key autonomous subsea observation platforms, are widely used in ocean environmental monitoring owing to their long endurance, ease of deployment, and wide-area coverage. The coupled effects of time-varying ocean currents and progressive biofouling, compounded by restricted underwater communication, constrain glider observations. The same coupling also leaves signatures in the onboard records, which can be used to reconstruct environmental fields and assess glider health. This paper proposes a physics-informed, adjoint-based dynamics inversion framework. A six-dimensional lumped disturbance vector is introduced to reformulate disturbance identification as a full-window optimal-tracking problem, and an adjoint-based windowed variational estimator is constructed to recover physically consistent environmental perturbations, thereby inferring quantities beyond those directly measured by the native sensor suite. Validation on operational glider data demonstrates that the framework reconstructs sparse, impulsive disturbances correlated with non-coordinated maneuvers, whose spectral and intermittency signatures are consistent with Kolmogorov inertial-subrange scaling and She–Lévêque anomalous scaling ($\zeta_6/\zeta_3 = 1.77$ versus the predicted 1.78). These disturbances also survive surrogate-data, noise-only, and model-error falsification tests of the full inversion pipeline. By coupling the identified disturbances with a viscous-moment inversion model, depth-resolved current retrieval is demonstrated without acoustic Doppler hardware. The depth-averaged component is cross-checked against the glide-angle method and two independent ocean reanalyses under an explicit uncertainty budget. Multi-profile analysis further reveals a statistically significant, monotonic drift in the glider's effective hydrodynamics over the deployment. The framework enables multi-dimensional environmental sensing and glider health assessment from low-cost onboard sensor data.

1. Introduction

Accurate characterization of key oceanic dynamical processes, such as mesoscale eddies and deep-ocean circulation, is crucial for understanding global climate change and marine ecosystems [1–4]. Existing observation networks, however, leave a persistent gap between the sea surface and the deep ocean. Satellite remote sensing offers broad coverage but captures only surface information [5], whereas in situ measurements from moored buoys and shipboard surveys are accurate but spatially sparse. Underwater gliders, with their low energy consumption, long endurance, multi-sensor integration, and near real-time data transmission, have become a key autonomous platform for filling this gap through sustained, three-dimensional monitoring of the marine environment [6, 7].

Exploiting this platform in increasingly diverse missions [8], however, places stringent demands on the fidelity of its dynamic model. Glider motion couples six-degree-of-freedom (6-DOF) rigid-body dynamics [9] with a variable-buoyancy propulsion system and strongly nonlinear hydrodynamics [10], and is further perturbed by practical factors such as progressive biofouling [11]. Restricted underwater communication [12] compounds the difficulty by precluding real-time correction, so these effects must instead be recovered from the onboard records after the mission. In the deep-sea flow environment, model uncertainty is therefore an intrinsic and largely irreducible feature [13], stemming both from limited knowledge of multi-scale coupling mechanisms and from simplifications required for computational tractability. Efforts to improve model accuracy have proceeded along two complementary pathways.

The first pathway raises the fidelity of forward modeling. Leonard and Graver [14] established the nonlinear vertical-plane model based on internal mass redistribution that underpins glider stability analysis and feedback control; Fan and Woolsey [15] incorporated non-uniform flow effects, showing that an accurate dynamic model in currents can itself reveal characteristics of the ambient flow; and Wang et al. [16] coupled deep neural networks with finite-element analysis to compensate for environmental factors in motion prediction. More recently, Wu et al. [17] optimized the motion trajectories of morphing gliders to balance energy

*Corresponding authors.
Email addresses: Zhang_Yong@tju.edu.cn (Y. Zhang); zhongkegao@tju.edu.cn (Z. Gao)
ORCID(s): 0000-0002-5759-6744 (Y. Zhang); 0000-0002-9551-202X (Z. Gao)
[1] These authors contributed equally to this work.

efficiency against motion accuracy, and Zang et al. [18] improved horizontal trajectory prediction by fusing dynamics-based inference with a fuzzy angle-of-attack representation.

The second pathway strengthens inverse identification from observed data. Yang et al. [19] combined expectation-maximization with particle filtering for robust identification of nonlinear state-space models subject to outliers and missing observations; Mao and He [20] characterized structural unidentifiability through the relationship between the Fisher information matrix and the Hessian; and Abdulsamad et al. [21] developed a Bayesian nonparametric mixture model for probabilistic learning of robotic inverse dynamics. These methods, however, target model parameters for control and leave unaddressed the environmental signals imprinted in the glider's motion.

Neither pathway, therefore, fully exploits the environmental information embedded in the dynamic coupling between the glider and the surrounding flow field. Fixed-parameter forward models cannot track time-varying effects such as biofouling accumulation and transient current shear, and existing inverse methods stop at control-oriented parameters. To close this gap, this paper proposes an adjoint-based dynamics inversion framework, in which disturbance identification is formulated as a full-window optimal-tracking problem and solved with adjoint-derived gradients. The estimator is a windowed variational one rather than a recursive observer. The framework recovers physically consistent environmental perturbations from standard onboard records and, on that basis, demonstrates depth-resolved current retrieval and characterizes the long-term drift of the glider's hydrodynamic parameters.

The contributions of this paper are threefold. (i) *Adjoint-based full-window identification of lumped disturbances*: unmodeled environmental and hydrodynamic effects are condensed into a six-dimensional lumped disturbance vector acting on the surge, sway, heave, roll, pitch, and yaw channels, and disturbance identification is reformulated as a full-window optimal-tracking problem on the full nonlinear 6-DOF dynamics, solved with adjoint-derived gradients. (ii) *Depth-resolved current retrieval*: inverting the identified yaw-channel disturbance through a viscous-moment model demonstrates the feasibility of retrieving depth-stratified currents without acoustic Doppler hardware, and the depth-averaged component, the only externally constrained one, is cross-checked against the glide-angle method and two independent ocean reanalyses under an explicit uncertainty budget. (iii) *Long-term hydrodynamic drift characterization*: tracking the identified parameters across the mission reveals a statistically significant, parameter-robust drift confined to the longitudinal plane, most plausibly a gradual change in the external hydrodynamic shape, indicating a route toward glider health monitoring from standard sensor data.

2. Preliminaries

2.1. Kinematics model

To describe the three-dimensional motion of the underwater glider, a 6-DOF kinematic framework is established using two reference frames, the inertial frame $E_0\{i, j, k\}$ and the body-fixed frame $B_0\{b_1, b_2, b_3\}$. The origin E_0 of the inertial frame is anchored at the mission deployment point, with its orthonormal basis vectors i, j, and k aligned with North, East, and along the direction of gravity (NED), respectively. The origin B_0 of the body-fixed frame coincides with the center of buoyancy of the glider, where the axes b_1, b_2, and b_3 form a right-handed system aligned with the longitudinal, transverse, and vertical axes of the glider.

Let the vector $\boldsymbol{\mu}_1 = [X, Y, Z]^T \in \mathbb{R}^3$ denote the position of the glider in the inertial frame, and $\boldsymbol{\mu}_2 = [\phi, \theta, \psi]^T \in \mathbb{R}^3$ represent its orientation expressed in Euler angles. The motion states in the body frame are defined by the linear velocity vector $\boldsymbol{V} = [u, v, w]^T \in \mathbb{R}^3$ and the angular velocity vector $\boldsymbol{\Omega} = [p, q, r]^T \in \mathbb{R}^3$. The 6-DOF kinematic equations of the glider are given by

$$\dot{\boldsymbol{\mu}}_1 = \boldsymbol{R}_{eb}\boldsymbol{V} \tag{1}$$

$$\dot{\boldsymbol{\mu}}_2 = \boldsymbol{I}_{eb}\boldsymbol{\Omega} \tag{2}$$

where $\boldsymbol{R}_{eb}$ and $\boldsymbol{I}_{eb}$ are the velocity and angular velocity transformation matrices from the body frame to the inertial frame, respectively, which are expressed as

$$\boldsymbol{R}_{eb} = \begin{bmatrix} c\theta c\psi & s\phi s\theta c\psi - c\phi s\psi & c\phi s\theta c\psi + s\phi s\psi \\ c\theta s\psi & s\phi s\theta s\psi + c\phi c\psi & c\phi s\theta s\psi - s\phi c\psi \\ -s\theta & s\phi c\theta & c\phi c\theta \end{bmatrix} \tag{3}$$

$$\boldsymbol{I}_{eb} = \begin{bmatrix} 1 & s\phi t\theta & c\phi t\theta \\ 0 & c\phi & -s\phi \\ 0 & s\phi/c\theta & c\phi/c\theta \end{bmatrix} \tag{4}$$

where $c(\cdot)$, $s(\cdot)$, and $t(\cdot)$ denote $\cos(\cdot)$, $\sin(\cdot)$, and $\tan(\cdot)$, respectively.

2.2. Dynamics model

Consider the underwater glider as a multi-body system with a constant total mass m, formulated to capture the dynamic coupling effects of internal moving masses. The system comprises four functional elements, namely the static hull m_h, the variable ballast m_b, the internal reservoir m_m, and the movable battery pack m_p. The static hull m_h constitutes the rigid assembly of the fuselage, wings, tail rudder, and fixed electronics, with the center of gravity located at $\boldsymbol{r}_h = [r_{h1}, r_{h2}, r_{h3}]^T$ relative to B_0.

The buoyancy adjustment system drives the glider by regulating net buoyancy through variations in the oil volume within the external bladder. This mechanism operates by transferring hydraulic oil between the internal reservoir and the external bladder. For the dynamic modeling, the fluid masses of the variable ballast and the internal reservoir are denoted by m_b and m_m, respectively. These masses are treated as point masses located at fixed positions $\boldsymbol{r}_b = [r_{b1}, r_{b2}, r_{b3}]^T$ and $\boldsymbol{r}_m = [r_{m1}, r_{m2}, r_{m3}]^T$ relative to B_0, characterizing the mass distribution of the working fluid.

The movable battery pack m_p actively shifts the center of gravity of the system relative to the fixed origin to generate the moments required for pitch and roll maneuvers. Let r_{px} denote the linear displacement of m_p along the b_1 axis, γ represent its rotation angle around the same axis, and R_p be the eccentricity radius. Consequently, with the total mass m remaining invariant, the instantaneous position vector of the movable battery pack relative to the center of buoyancy B_0 is expressed as

$$\boldsymbol{r}_p = [r_{p1} + r_{px}, R_p \sin\gamma, R_p \cos\gamma]^T \tag{5}$$

Using the Newton-Euler method [22–24], we express the dynamic model of the glider as

$$\boldsymbol{M} \begin{bmatrix} \dot{\boldsymbol{V}} \\ \dot{\boldsymbol{\Omega}} \end{bmatrix} = \begin{bmatrix} \boldsymbol{P} \times \boldsymbol{\Omega} \\ \boldsymbol{\Pi} \times \boldsymbol{\Omega} + \boldsymbol{P} \times \boldsymbol{V} \end{bmatrix} + \begin{bmatrix} \boldsymbol{F}_{ext} \\ \boldsymbol{M}_{ext} \end{bmatrix} \tag{6}$$

where $\boldsymbol{F}_{ext}$ and $\boldsymbol{M}_{ext}$ denote the external forces and moments, respectively. $\boldsymbol{P}$ and $\boldsymbol{\Pi}$ represent the total linear momentum and angular momentum, respectively. The total inertia matrix $\boldsymbol{M}$ is the sum of the rigid-body inertia matrix $\boldsymbol{M}_{RB}$ and the added mass matrix $\boldsymbol{M}_f$, defined as

$$\boldsymbol{M}_{RB} = \mathrm{diag}(m\boldsymbol{I}_{3\times3}, \boldsymbol{J}_f) \tag{7}$$

$$\boldsymbol{M}_f = \mathrm{diag}(M_{f1}, M_{f2}, M_{f3}, I_{f1}, I_{f2}, I_{f3}) \tag{8}$$

Here, $\boldsymbol{J}_f = \mathrm{diag}(J_x, J_y, J_z)$ is the rigid-body inertia tensor, and $\boldsymbol{I}_{3\times3}$ is the identity matrix. The total linear momentum $\boldsymbol{P}$ and angular momentum $\boldsymbol{\Pi}$, which incorporate the coupling effects of the internal moving masses, are formulated as

$$\begin{bmatrix} \boldsymbol{P} \\ \boldsymbol{\Pi} \end{bmatrix} = \boldsymbol{M}_f \begin{bmatrix} \boldsymbol{V} \\ \boldsymbol{\Omega} \end{bmatrix} + \begin{bmatrix} \sum_i m_i(\boldsymbol{V} + \boldsymbol{\Omega} \times \boldsymbol{r}_i) \\ \sum_i m_i \boldsymbol{r}_i \times (\boldsymbol{V} + \boldsymbol{\Omega} \times \boldsymbol{r}_i) \end{bmatrix} \tag{9}$$

where $i \in \{b, p, h, m\}$ iterates over the sub-components. In Eq. (6), $\boldsymbol{F}_{ext}$ and $\boldsymbol{M}_{ext}$ denote the external forces and moments, respectively, which include buoyancy, gravity, and hydrodynamic effects. Let $\boldsymbol{F}_g$ and $\boldsymbol{T}_g$ denote the net buoyancy and gravitational forces and moments, calculated as

$$\begin{bmatrix} \boldsymbol{F}_g \\ \boldsymbol{T}_g \end{bmatrix} = \begin{bmatrix} (m_x g - F_z)\boldsymbol{R}_{eb}^k \\ (m_h \boldsymbol{r}_h + m_p \boldsymbol{r}_p + m_b \boldsymbol{r}_b + m_m \boldsymbol{r}_m) \times (g\boldsymbol{R}_{eb}^k) \end{bmatrix} \tag{10}$$

where $m_x = m_b + m_m$, g is gravitational acceleration, and $\boldsymbol{R}_{eb}^k$ represents the unit vector of the inertial gravity direction transformed into the body frame. F_z is defined as the depth-dependent buoyancy compensation force.

The viscous hydrodynamic forces $\boldsymbol{F}_v$ and moments $\boldsymbol{M}_v$ acting on the underwater glider are defined in the flow frame as $\boldsymbol{F}_v = [-D, SF, -L]^T$ and $\boldsymbol{M}_v = [M_{DL1}, M_{DL2}, M_{DL3}]^T$, respectively. Following Zhang et al. [25], these terms are transformed into the body frame as

$$\boldsymbol{F}_v = \boldsymbol{R}_{bf} \begin{bmatrix} -D \\ SF \\ -L \end{bmatrix} = \boldsymbol{R}_{bf} V_b^2 \begin{bmatrix} -K_{D0} - K_D\alpha^2 \\ K_\beta \beta \\ -K_L \alpha \end{bmatrix} \tag{11}$$

$$\boldsymbol{M}_v = \boldsymbol{R}_{bf} \begin{bmatrix} M_{DL1} \\ M_{DL2} \\ M_{DL3} \end{bmatrix} = \boldsymbol{R}_{bf} V_b^2 \begin{bmatrix} K_{MR}\beta + K_p p \\ K_{M0} + K_M \alpha + K_q q \\ K_{MY}\beta + K_r r \end{bmatrix} \tag{12}$$

where K with a subscript denotes the viscous hydrodynamic coefficient. The speed V_b, angle of attack α, and sideslip angle β are calculated by

$$\begin{cases} V_b = \sqrt{u^2 + v^2 + w^2} \\ \alpha = \tan^{-1}(w/u) \\ \beta = \sin^{-1}(v/V_b) \end{cases} \tag{13}$$

Finally, the flow-to-body rotation matrix $\boldsymbol{R}_{bf}$ is given by

$$\boldsymbol{R}_{bf} = \begin{bmatrix} \cos\alpha\cos\beta & -\cos\alpha\sin\beta & -\sin\alpha \\ \sin\beta & \cos\beta & 0 \\ \sin\alpha\cos\beta & -\sin\alpha\sin\beta & \cos\alpha \end{bmatrix} \tag{14}$$

3. Model Validation and Performance Analysis

We validate the established model against actual sea-trial data. The data show that ocean currents strongly affect the glider's motion trajectory, navigation efficiency, and mission capability over long-duration deployments.

3.1. Experimental Data and Benchmark Establishment

The experimental data used in this study were collected in April 2023 in the South China Sea using a Petrel-L long-range underwater glider. The hydrodynamic parameters and physical specifications of the glider are taken from Wang et al. [9]. During validation, the depth-dependent buoyancy parameter is set as $m_z = Z/200$. The mission lasted 69 days and 17 hours, yielding 565 profiles. The glider was equipped with a conductivity-temperature-depth (CTD) sensor and a Tilt-Compensated Compass Module 3 (TCM3) digital compass, which provided depth and attitude measurements, respectively.

Since the glider cannot receive GPS signals while submerged, it obtains a position fix only upon surfacing. To reconstruct a continuous horizontal trajectory for comparison, we use the method described in Zhou et al. [22].

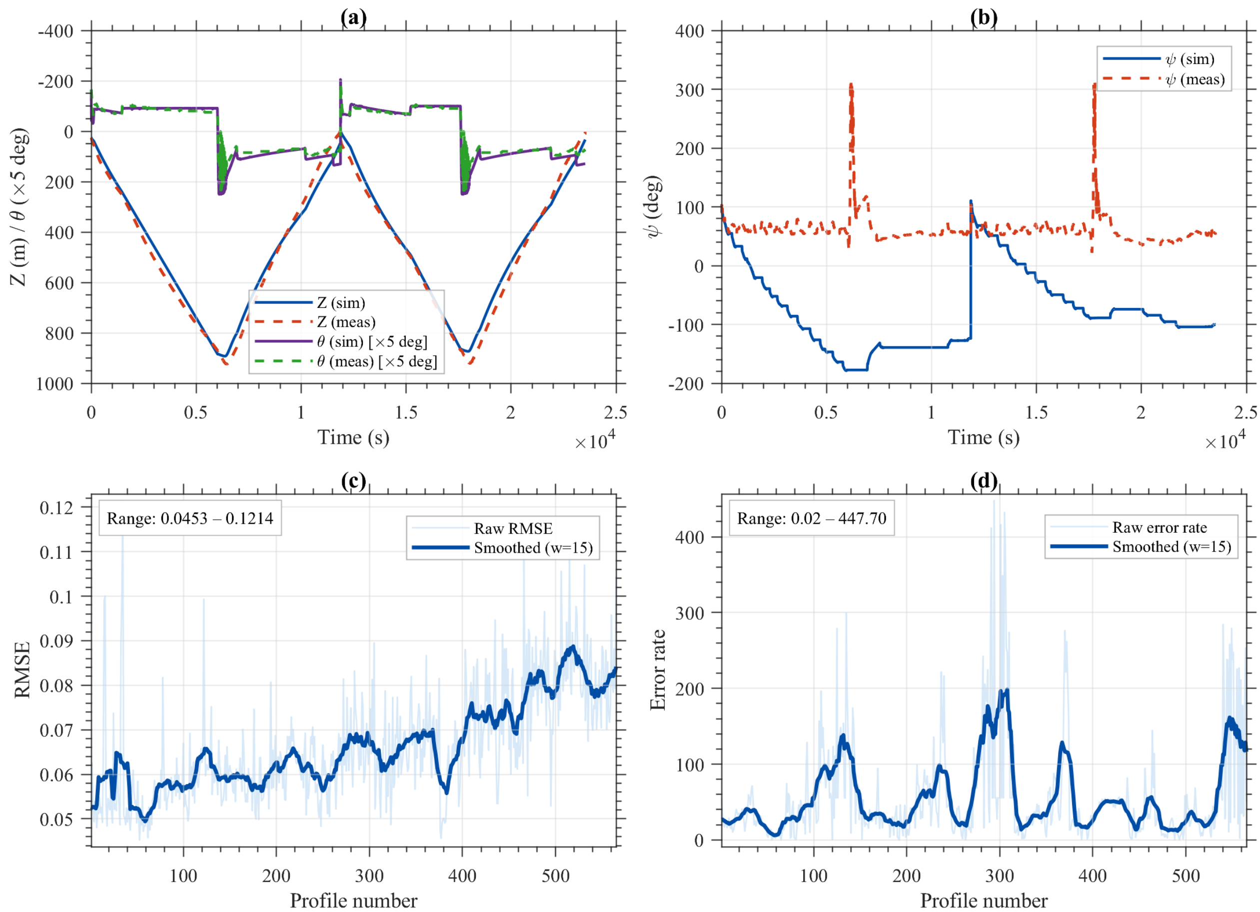

Figure 1: Model validation against sea-trial data. (a) Vertical dynamics: depth and pitch angle; (b) heading angle comparison; (c) longitudinal RMSE evolution; (d) horizontal position error rate over the mission duration.

This method combines data from the CTD sensor and the TCM3 compass to estimate the glider's horizontal velocity, which is then integrated to derive the trajectory. This estimated path serves as the baseline for evaluating the model's performance. This dead-reckoning benchmark is itself only an approximation. The glide-angle relation assumes quasi-steady flight and neglects unsteady added-mass effects and the depth-dependent current within the water column, so it carries a systematic error of its own and is used here only as a qualitative reference.

Based on this method, the horizontal velocity v_g is calculated as $v_g = v_z / \tan\xi$, where v_z is the vertical velocity obtained by differentiating the CTD depth data, and ξ is the gliding angle, defined as the difference between the pitch angle θ and the angle of attack α. The angle of attack α is given by

$$\alpha = \frac{K_L}{2K_D}\tan\xi\left(\sqrt{1 - 4\frac{K_D}{K_L^2}\cot\xi\left(K_{D0}\cot\xi\right)} - 1\right) \quad (15)$$

3.2. Results and Analysis

To validate the dynamics model from Section 2, we used the recorded control variables to simulate the glider pose. We then compared these simulation results with the sensor data and the estimated-trajectory benchmark from Section 3.1. The validation results are presented in Fig. 1, covering the local dynamic response in Fig. 1(a, b) and the global statistical error in Fig. 1(c, d).

Vertical Dynamics: Fig. 1(a) compares the depth and pitch angle for two continuous profiles. While the depth trajectory shows high agreement between model predictions and measured data, a closer inspection reveals that the pitch-angle fit is not entirely precise. Specifically, the simulated pitch angle exhibits depth-dependent deviations that do not perfectly track the fluctuations observed in the actual data. This discrepancy suggests that the local dynamic characteristics of the static model do not fully match the real-world motion of the glider. Such inaccuracies in pitch estimation affect the decomposition of velocity vectors and can accumulate into errors in position and speed estimation.

Furthermore, Fig. 1(c) reveals a slight but clear upward trend in the RMSE over time, indicating a gradual degradation in model accuracy. This trend points to a progressive change in the effective hydrodynamic profile over long-duration operation, a time-varying effect not captured by the fixed-parameter model.

Horizontal Dynamics: The predicted heading angle in Fig. 1(b) shows a systematic offset relative to the measured data, and Fig. 1(d) reveals a periodically varying deviation between the predicted and actual surfacing positions. These errors are primarily attributed to unmodeled lateral environmental disturbances, particularly ocean currents, whose continuous effect on the horizontal trajectory accumulates over time.

The above results reveal two principal sources of model-measurement discrepancy during long-term deployment. The first is a progressive change in the effective hydrodynamics that degrades vertical prediction accuracy, and the second is cumulative horizontal drift introduced by unmodeled ocean currents. Accurate identification and compensation of these environmental factors would both improve model fidelity and extend the observational capabilities of underwater gliders.

4. Optimal Control and Disturbance Inversion Framework

Motivated by the model-measurement discrepancies identified in the preceding section, a disturbance inversion framework is developed to systematically recover and compensate for the unmodeled environmental effects. The environmental influence acting on the glider during a dive is decomposed into two parts. The first comprises the intermittent horizontal disturbances that perturb the submerged dynamics, and the second is a depth-averaged translational drift that cannot be directly observed by the onboard sensors. To describe the sensor-observable component in a unified manner, unmodeled factors, including ocean-current shear, progressive biofouling, and model-parameter mismatch, are represented by a six-dimensional lumped disturbance vector acting on the surge, sway, heave, roll, pitch, and yaw channels. A disturbance-augmented EKF first supplies a coarse prior for these channels. The identification is then recast as an adjoint-based optimal control problem, with the adjoint equations and gradients derived from variational principles. An adaptive sliding-window strategy suppresses the boundary artifacts that segmented optimization introduces over long trajectories. The optimized terminal dynamics are then combined with the resurfaced GPS position to estimate the depth-averaged current, which remains unobservable during submergence.

4.1. Disturbance-Augmented Dynamics and EKF Prior Estimation

To enable simultaneous state and disturbance estimation, the 12-dimensional state vector, the six-dimensional lumped disturbance vector, and their augmented form are defined as

$$\boldsymbol{y} = [\phi, \theta, \psi, X, Y, Z, u, v, w, p, q, r]^T \in \mathbb{R}^{12} \tag{16}$$

$$\boldsymbol{b}_c = [B_{cu}, B_{cv}, B_{cw}, B_{cp}, B_{cq}, B_{cr}]^T \in \mathbb{R}^6 \tag{17}$$

$$\boldsymbol{x} = [\boldsymbol{y}^T, \boldsymbol{b}_c^T]^T \in \mathbb{R}^{18} \tag{18}$$

Under the assumption that the unmodeled disturbances evolve locally as a random walk process, the continuous-time nonlinear augmented system dynamics take the form

$$\dot{x}(t) = f_{aug}(x(t), t) + w(t) = \begin{bmatrix} F(y(t), b_c(t), t) \\ \mathbf{0}_{6\times 1} \end{bmatrix} + w(t) \tag{19}$$

where $F(\cdot)$ denotes the original 12-dimensional nonlinear dynamic equations, and $w(t)$ is the continuous process noise vector. Incorporating the disturbance terms into each channel gives the augmented dynamics

$$\begin{cases} \dot{u} = f_7 + B_{cu}/(m + M_{f1}) \\ \dot{v} = f_8 + B_{cv}/(m + M_{f2}) \\ \dot{w} = f_9 + B_{cw}/(m + M_{f3}) \\ \dot{p} = f_{10} + B_{cp}/(J_x + I_{f1}) \\ \dot{q} = f_{11} + B_{cq}/(J_y + I_{f2}) \\ \dot{r} = f_{12} + B_{cr}/(J_z + I_{f3}) \end{cases} \tag{20}$$

Each component of $\boldsymbol{b}_c$ can be interpreted as a channel-wise residual force or moment, although each component may combine several physical effects. Because the disturbance enters every channel additively, it absorbs effects that the nominal model omits. The affected channel indicates which dynamic balance the residual contributes to most. It does not identify a single physical source. The longitudinal-plane terms collect the streamwise and vertical force contributions. The surge disturbance B_{cu} aggregates parasitic-drag growth together with buoyancy-engine residuals. The heave disturbance B_{cw} reflects departures of the lift-buoyancy balance, and the pitch moment B_{cq} captures migration of the hydrodynamic pressure center. The lateral-plane terms carry the cross-track forcing. The sway force B_{cv} and the yaw moment B_{cr} respond chiefly to ocean-current shear acting transverse to the hull, whereas the roll moment B_{cp} reflects residual roll asymmetry. A given component thus aggregates environmental forcing, hydrodynamic-parameter uncertainty, and biofouling-related change. These contributions are kept combined at the modeling stage and disentangled a posteriori by their differing temporal and spectral signatures.

With a fixed sampling time step h_t, numerical integration discretizes the system into the state transition and measurement equations

$$x_k = f_d(x_{k-1}) + w_{k-1} \tag{21}$$

$$z_k = H x_k + v_k \tag{22}$$

where the subscript k denotes the discrete time step and $f_d(\cdot)$ is the discrete-time state transition function. The measurement vector $z_k \in \mathbb{R}^4$ comprises the attitude and depth readings acquired by the onboard sensors, namely $z_k = [\phi_g, \theta_g, \psi_g, Z_g]^T$. The constant matrix $H \in \mathbb{R}^{4\times 18}$ is a linear observation matrix that maps the augmented state x_k into the measurement space. $w_{k-1} \sim \mathcal{N}(0, Q_k)$

and $v_k \sim \mathcal{N}(0, R_k)$ denote the discrete process and measurement noises, respectively, both modeled as zero-mean Gaussian white noise with covariance matrices Q_k and R_k.

The EKF recursively estimates the augmented state through the standard prediction-update cycle. In the prediction step

$$\hat{x}_{k|k-1} = f_d(\hat{x}_{k-1|k-1}) \tag{23}$$

$$P_{k|k-1} = \Phi_{k-1} P_{k-1|k-1} \Phi_{k-1}^T + Q_{k-1} \tag{24}$$

where $\hat{x}_{k|k-1}$ is the a priori augmented state estimate, $P_{k|k-1}$ is the a priori error covariance matrix, and $\Phi_{k-1} = \frac{\partial f_d}{\partial x}\Big|_{x=\hat{x}_{k-1|k-1}}$ is the Jacobian matrix of the nonlinear system dynamics evaluated at the previous state estimate. In the update step

$$K_k = P_{k|k-1} H^T (H P_{k|k-1} H^T + R_k)^{-1} \tag{25}$$

$$\hat{x}_{k|k} = \hat{x}_{k|k-1} + K_k (z_k - H \hat{x}_{k|k-1}) \tag{26}$$

$$P_{k|k} = (I_{18\times18} - K_k H) P_{k|k-1} \tag{27}$$

where K_k is the Kalman gain matrix, $\hat{x}_{k|k}$ is the refined a posteriori state estimate, and $I_{18\times18}$ denotes the identity matrix.

Forward recursive iterations over the mission profile yield a coarse disturbance prior $\hat{b}_c^{EKF}(t)$ that effectively captures slowly varying components such as depth-compensation drift, while exhibiting delay and attenuation for abrupt impulsive disturbances. The EKF output is therefore retained solely as a dynamically consistent initial estimate for the subsequent adjoint optimization.

4.2. Adjoint-Based Optimal-Tracking Formulation

To fix terminology, the adjoint-based optimal-tracking formulation developed in this subsection is an optimal-control problem in which the model output tracks the measured attitude and depth. It is the core optimization step of the overall adjoint-based dynamics inversion framework, abbreviated adjoint-based inversion where the context is unambiguous. The former denotes the per-window optimal-tracking sub-problem, and the latter the end-to-end identification pipeline comprising the EKF prior, the adjoint optimal-tracking step, the sliding-window strategy, and the current and long-term drift inversion. These terms are used consistently in this sense throughout the paper.

In the adjoint optimization initialization, the longitudinal-plane disturbances are set to the EKF estimate, $b_{c,\mathrm{lon}}^{(0)}(t) = \hat{b}_{c,\mathrm{lon}}^{EKF}(t)$, whereas the lateral-plane disturbances are initialized to zero, $b_{c,\mathrm{lat}}^{(0)}(t) = \mathbf{0}$. The disturbance identification is then recast as a full-window optimal-tracking problem, enabling the adjoint solver to reconstruct temporally concentrated disturbances from the full trajectory.

The identification problem is cast as an optimal control problem that seeks the input sequence $\boldsymbol{b}_c^*(t)$ minimizing the cost functional $\boldsymbol{J}$, which measures the deviation between the dynamic-model output $\boldsymbol{y}$ and the measured data $\boldsymbol{y}_g$. The cost functional is defined as

$$\begin{aligned} \boldsymbol{J} = \int_0^T & \left[(\phi(t) - \phi_g)^2 + (\theta(t) - \theta_g)^2 + (\psi(t) - \psi_g)^2 \right. \\ & \left. + (Z(t) - Z_g)^2 \right] dt \end{aligned} \tag{28}$$

where ϕ_g, θ_g, ψ_g, and Z_g denote the attitude angles and depth measured by the onboard sensors, respectively. The cost functional is restricted to the attitude and depth channels because horizontal positions are not directly observable during submersion. Writing the bracketed integrand as the running cost $\ell(\boldsymbol{y}) = (\phi - \phi_g)^2 + (\theta - \theta_g)^2 + (\psi - \psi_g)^2 + (Z - Z_g)^2$, the cost reads $\boldsymbol{J} = \int_0^T \ell \, dt$, and the pointwise optimality conditions below are expressed through ℓ.

The optimal control input $\boldsymbol{b}_c^*(t)$ and the resulting optimal state evolution $\boldsymbol{y}^*(t)$ must satisfy the first-order necessary conditions for optimality. These conditions are derived by minimizing the augmented Lagrangian functional L, defined as

$$L(\boldsymbol{y}, \boldsymbol{b}_c, \lambda) = \boldsymbol{J}(\boldsymbol{y}) + \int_0^T \lambda^\top (\boldsymbol{F}(\boldsymbol{y}, \boldsymbol{b}_c, t) - \dot{\boldsymbol{y}}) dt \tag{29}$$

where λ is the Lagrange multiplier vector. The first variation of L with respect to independent variations of the state $\delta \boldsymbol{y}$ and the control $\delta \boldsymbol{b}_c$ is given by

$$\begin{aligned} \delta L = \int_0^T & \left[\left(\frac{\partial \ell}{\partial \boldsymbol{y}} \right)^\top \delta \boldsymbol{y} + \lambda^\top \frac{\partial \boldsymbol{F}}{\partial \boldsymbol{y}} \delta \boldsymbol{y} \right. \\ & \left. + \lambda^\top \frac{\partial \boldsymbol{F}}{\partial \boldsymbol{b}_c} \delta \boldsymbol{b}_c - \lambda^\top \delta \dot{\boldsymbol{y}} \right] dt \end{aligned} \tag{30}$$

The variation with respect to $\delta \boldsymbol{y}$ yields the adjoint equation and its boundary condition, while the variation with respect to $\delta \boldsymbol{b}_c$ yields the cost gradient. Applying integration by parts to the last term, $\int_0^T \lambda^\top (-\delta \dot{\boldsymbol{y}}) \, dt$, yields

$$\int_0^T \lambda^\top (-\delta \dot{\boldsymbol{y}}) dt = - \lambda^\top \delta \boldsymbol{y} \Big|_0^T + \int_0^T \dot{\lambda}^\top \delta \boldsymbol{y} dt \tag{31}$$

Setting $\delta L / \delta \boldsymbol{y} = 0$ and collecting the terms associated with $\delta \boldsymbol{y}$ yields

$$\int_0^T \left[\left(\frac{\partial \ell}{\partial \boldsymbol{y}} \right)^\top + \lambda^\top \frac{\partial \boldsymbol{F}}{\partial \boldsymbol{y}} + \dot{\lambda}^\top \right] \delta \boldsymbol{y} \, dt - \lambda^\top \delta \boldsymbol{y} \Big|_0^T = 0 \tag{32}$$

Since the integral must vanish for any variation $\delta \boldsymbol{y}(t)$, the integrand itself must be identically zero. The resulting adjoint equation is

$$\dot{\lambda}(t) = -\left(\frac{\partial \ell}{\partial \boldsymbol{y}}\right)^{\mathsf{T}} - \left(\frac{\partial \boldsymbol{F}}{\partial \boldsymbol{y}}\right)^{\mathsf{T}} \lambda$$
$$= 2\begin{bmatrix} \phi_g - \phi \\ \theta_g - \theta \\ \psi_g - \psi \\ 0 \\ 0 \\ Z_g - Z \\ 0 \\ \vdots \\ 0 \end{bmatrix} - \begin{bmatrix} \frac{\partial f_1}{\partial y_1} & \cdots & \frac{\partial f_{12}}{\partial y_1} \\ \vdots & \ddots & \vdots \\ \frac{\partial f_1}{\partial y_{12}} & \cdots & \frac{\partial f_{12}}{\partial y_{12}} \end{bmatrix} \lambda \tag{33}$$

Here $\partial \boldsymbol{F}/\partial \boldsymbol{y}$ is the analytic Jacobian of the twelve right-hand sides evaluated along the forward trajectory, obtained in closed form by symbolic differentiation.

Additionally, the boundary term must satisfy the transversality condition. Because the initial state $\boldsymbol{y}(0) = \boldsymbol{y}_0$ is prescribed, the lower-limit variation vanishes, $\delta\boldsymbol{y}(0) = \boldsymbol{0}$, whereas the terminal state $\boldsymbol{y}(T)$ is free, so the boundary term reduces to

$$-\lambda^{\mathsf{T}}\delta\boldsymbol{y}\Big|_0^T = -\lambda^{\mathsf{T}}(T)\delta\boldsymbol{y}(T) = 0 \tag{34}$$

Since $\delta\boldsymbol{y}(T)$ is arbitrary, the terminal condition for the adjoint variable is $\lambda(T) = \boldsymbol{0}$. This structure is forward-backward in time: the state equation $\dot{\boldsymbol{y}} = \boldsymbol{F}(\cdot)$ evolves forward from the initial condition $\boldsymbol{y}_0$, while the adjoint equation propagates backward from the terminal condition $\lambda(T) = \boldsymbol{0}$. The backward propagation maps the gradient of the state deviation to the initial time, which enables identification of the disturbance vector $\boldsymbol{b}_c(t)$.

With the costate determined by the adjoint equation and its terminal condition, the gradient required by the optimization follows from the variation of L with respect to the control. Since the cost penalizes only the states, the explicit term $\partial \ell/\partial \boldsymbol{b}_c$ vanishes, and the reduced gradient is obtained as

$$\nabla_{\boldsymbol{b}_c} \boldsymbol{J} = \frac{\partial \ell}{\partial \boldsymbol{b}_c} + \left(\frac{\partial \boldsymbol{F}}{\partial \boldsymbol{b}_c}\right)^{\mathsf{T}} \lambda = \left(\frac{\partial \boldsymbol{F}}{\partial \boldsymbol{b}_c}\right)^{\mathsf{T}} \lambda \tag{35}$$

A single backward integration of λ thus replaces the six forward sensitivity integrations that a direct evaluation of $\partial \boldsymbol{y}/\partial \boldsymbol{b}_c$ would otherwise require, which is the central economy of the adjoint method. Because the disturbance acts affinely on only the six velocity and angular-rate equations, the input Jacobian $\partial \boldsymbol{F}/\partial \boldsymbol{b}_c$ is constant, with a zero kinematic block and a lower block that is diagonal in the reciprocal effective masses and inertias of the six channels. The gradient therefore reduces to a channel-wise scaling of the velocity and angular-rate costates, expressed as

$$\nabla_{\boldsymbol{b}_c} \boldsymbol{J} = \begin{bmatrix} \lambda_u/(m + M_{f1}) \\ \lambda_v/(m + M_{f2}) \\ \lambda_w/(m + M_{f3}) \\ \lambda_p/(J_x + I_{f1}) \\ \lambda_q/(J_y + I_{f2}) \\ \lambda_r/(J_z + I_{f3}) \end{bmatrix} \tag{36}$$

where $(\lambda_u, \lambda_v, \lambda_w, \lambda_p, \lambda_q, \lambda_r)$ denote the costates of the body-frame velocities and angular rates. The first-order necessary condition for a stationary point of the windowed cost is $\nabla_{\boldsymbol{b}_c} \boldsymbol{J} = \boldsymbol{0}$.

The state equation, the adjoint equation, and the gradient admit a compact Hamiltonian form. With the Hamiltonian $H(\boldsymbol{y}, \boldsymbol{b}_c, \lambda, t) = \ell(\boldsymbol{y}) + \lambda^{\mathsf{T}}\boldsymbol{F}(\boldsymbol{y}, \boldsymbol{b}_c, t)$ and the running cost ℓ defined above, these are given by

$$\begin{aligned} &\dot{\boldsymbol{y}} = \frac{\partial H}{\partial \lambda}, \qquad \dot{\lambda} = -\frac{\partial H}{\partial \boldsymbol{y}}, \qquad \lambda(T) = \boldsymbol{0}, \\ &\nabla_{\boldsymbol{b}_c} \boldsymbol{J} = \frac{\partial H}{\partial \boldsymbol{b}_c} \end{aligned} \tag{37}$$

These constitute first-order necessary conditions for local optimality, and global optimality is not claimed, since the cost is non-convex in $\boldsymbol{b}_c$ through the nonlinear flow map.

For the numerical solution, the window $[0, T]$ is discretized into N steps of size h_t. Given the current disturbance estimate, the state is integrated forward from $\boldsymbol{y}_0$. The adjoint is then integrated backward from $\lambda(T) = \boldsymbol{0}$ with a first-order-consistent scheme on the same step, and the gradient is assembled channel-wise from the resulting costates. The pair $(\boldsymbol{J}, \nabla_{\boldsymbol{b}_c} \boldsymbol{J})$ is supplied to a gradient-based quasi-Newton optimizer, an interior-point method with a limited-memory BFGS Hessian approximation, which updates $\boldsymbol{b}_c$ until the first-order optimality tolerance is met, yielding the windowed stationary solution $\boldsymbol{b}_c^*(t)$.

4.3. Segmented Full-Window Hybrid Optimization Strategy

The disturbance over a full dive is recovered by applying the windowed adjoint solve of the preceding subsection segment by segment and stitching the segments with an adaptive handover. Directly applying the optimal control formulation over the entire trajectory $[0, T]$ poses significant computational challenges. On long timescales the state space is high-dimensional, which creates an excessive computational burden and makes global convergence numerically intractable. Moreover, the glider's internal actuation, which adjusts buoyancy and the center of mass, induces mechanical vibrations that intermittently degrade sensor reliability. Treating the trajectory as a single continuous block risks allowing local data anomalies to corrupt the global solution. A segmented optimization approach therefore divides the problem into manageable sub-intervals and isolates the vibration-induced noise within individual segments, which improves the feasibility of the solution.

However, a straightforward segmentation strategy, while resolving the dimensionality issue, may introduce significant numerical instability. Optimizing each segment as an independent free-terminal problem artificially imposes a zero terminal adjoint, $\lambda(t_{i+1}) = \mathbf{0}$, at every interior boundary, whereas the full-window problem carries a generally nonzero adjoint, $\lambda(t_{i+1}) \neq \mathbf{0}$, there. Under direct state handover, the terminal state of the current segment $\boldsymbol{y}^*(t_{i+1})$ is strictly imposed as the initial condition of the next segment, $\boldsymbol{y}_{init}^{(i+1)} = \boldsymbol{y}^*(t_{i+1})$, so this boundary mismatch propagates downstream and compels the optimizer to generate abrupt, high-magnitude control inputs $\boldsymbol{b}_c(t)$ at the onset of the new segment.

To address these challenges, an adaptive sliding-window optimization strategy is proposed. The strategy dynamically regulates the state transition between segments according to the quality of local optimization. Let $\boldsymbol{J}_i^*$ denote the minimized cost for the i-th interval $[t_i, t_{i+1}]$, τ_c a predefined cost threshold, and $\mathcal{T}_{shake}$ the set of time instances affected by known vibrations. The initial condition for the subsequent segment $\boldsymbol{y}_{init}^{(i+1)}$ is determined by the following adaptive rule

$$\boldsymbol{y}_{init}^{(i+1)} = \begin{cases} \boldsymbol{y}^*(t_{i+1} - \Delta t_{slide}) & \text{if } \boldsymbol{J}_i^* < \tau_c \text{ and } t_{i+1} \notin \mathcal{T}_{shake} \\ \boldsymbol{y}^*(t_{i+1}) & \text{otherwise} \end{cases} \tag{38}$$

When the local optimization achieves high quality, $\boldsymbol{J}_i^* < \tau_c$, and the terminal data are reliable, $t_{i+1} \notin \mathcal{T}_{shake}$, the initial condition is retracted by a time margin Δt_{slide} to a state of higher confidence. This retraction enhances stability by bypassing the terminal region where numerical artifacts are most pronounced. Conversely, if the cost exceeds the threshold or a vibration-affected node is encountered, the algorithm reverts to direct handover to accommodate local convergence limitations or to process known data anomalies. When a window's cost stays above τ_c, the next segment falls back to direct handover, which prevents an occasional poorly converged window from contaminating its successors and lets the inversion re-converge within a few windows. The attitude-adjustment intervals flagged by $\mathcal{T}_{shake}$ are likewise removed before the steady-glide statistics are formed.

The complete procedure, from the EKF initialization through the per-window adjoint solve to the sliding-window handover, is summarized in Algorithm 1.

4.4. Depth-Averaged Current Estimation

After the adjoint optimization yields the refined disturbance vector $\boldsymbol{b}_c^*(t)$, the dynamics are forward-integrated with zero drift to obtain a reference trajectory. The residual displacement between the simulated resurfacing point and the GPS fix is attributed to the depth-averaged current, which manifests as an accumulated translational drift that is not observable by the onboard attitude and depth sensors.

To capture variation in current effects across dive phases, the profile is segmented at each dive-climb cycle boundary, detected automatically when the measured depth crosses a near-surface threshold ($Z_{\text{thr}} = 0.05 \cdot \max|Z|$) from below. For the k-th segment with duration $\Delta T_k = (n_{k+1} - n_k)\, h_t$, the drift velocity is computed as

$$V_{d,X}^{(k)} = \frac{\Delta X_{\text{GPS}} \cdot \Delta T_k / T_{\text{dive}} - [X_{\text{raw}}(n_{k+1}) - X_{\text{raw}}(n_k)]}{\Delta T_k} \tag{39}$$

$$V_{d,Y}^{(k)} = \frac{\Delta Y_{\text{GPS}} \cdot \Delta T_k / T_{\text{dive}} - [Y_{\text{raw}}(n_{k+1}) - Y_{\text{raw}}(n_k)]}{\Delta T_k} \tag{40}$$

where $(\Delta X_{\text{GPS}}, \Delta Y_{\text{GPS}})$ is the total GPS displacement between the entry and resurfacing points, T_{dive} is the total dive duration, and $(X_{\text{raw}}, Y_{\text{raw}})$ are the horizontal coordinates of the drift-free reference trajectory. By construction the segment drifts close on the GPS residual, $\sum_k \boldsymbol{V}_d^{(k)}\, \Delta T_k = \Delta \boldsymbol{X}_{\text{GPS}} - [\boldsymbol{X}_{\text{raw}}(T_{\text{dive}}) - \boldsymbol{X}_{\text{raw}}(0)]$, so the drift displacement they accumulate exactly reproduces the total GPS residual.

The two stages match what each measurement can observe. The onboard sensors carry enough information to identify $\boldsymbol{b}_c^*(t)$ by adjoint inversion, while the depth-averaged current can be observed only from the resurfacing GPS boundary condition. A uniform-drift assumption forces a single drift velocity over the whole profile. Segmented estimation instead lets each dive-climb cycle carry its own drift velocity, so it captures how the current acts differently at different depths.

5. Verification

To validate the proposed adjoint-based dynamics inversion framework, experimental verification was conducted using the sea-trial data described in Section 3. The verification builds from a single profile to the full mission. Reconstruction fidelity on a single profile is established first, together with the computational cost and parameter sensitivity of the windowed solver, and the inversion is then contrasted with an EKF baseline to expose the temporal resolution that separates the two. Surrogate-data, noise-only, and model-error falsification tests then probe the spectral and intermittency structure to establish whether the identified high-frequency disturbance is physical. The characterized disturbance is next applied to retrieve a depth-resolved current profile, whose depth-averaged component is cross-validated against the glide-angle method and two independent ocean reanalyses. Tracking the identified disturbance parameters across the full deployment finally reveals their long-term drift.

5.1. Single-Profile Verification

5.1.1. State Reconstruction

Under nominal conditions, the fidelity with which the proposed optimization framework reconstructs the sensor-observable states is verified first. To this end, Profile 18 from the initial deployment phase is examined, an early stage with a relatively stable flow field and a clean hull whose hydrodynamics remain close to the nominal model. For rigorous validation, the a priori depth-compensation parameter m_z is

Algorithm 1 Segmented full-window adjoint disturbance inversion

Require: measurements $\boldsymbol{y}_g(t)$ on $[0, T]$, initial state $\boldsymbol{y}_0$, EKF prior $\hat{\boldsymbol{b}}_c^{EKF}$, window length T_{seg}, slide margin Δt_{slide}, cost threshold τ_c, vibration set $\mathcal{T}_{shake}$

Ensure: refined disturbance field $\boldsymbol{b}_c^*(t)$

initialize $\boldsymbol{b}_c$ with the longitudinal channels set to $\hat{\boldsymbol{b}}_c^{EKF}$ and the lateral channels to zero
partition $[0, T]$ into successive windows of length T_{seg} and set $\boldsymbol{y}_{init}^{(1)} \leftarrow \boldsymbol{y}_0$
for each window i **do**
    repeat
        integrate the state forward from $\boldsymbol{y}_{init}^{(i)}$ under the current $\boldsymbol{b}_c$
        integrate the adjoint backward from $\lambda(t_{i+1}) = \mathbf{0}$
        assemble the channel-wise gradient $\nabla_{\boldsymbol{b}_c} \boldsymbol{J}$ from the costates
        update $\boldsymbol{b}_c$ on the window by an interior-point quasi-Newton step with an L-BFGS Hessian
    until the first-order optimality measure falls below tolerance
    store the window solution $\boldsymbol{b}_c^*$ on $[t_i, t_{i+1}]$ and its cost J_i^*
    if $J_i^* < \tau_c$ and $t_{i+1} \notin \mathcal{T}_{shake}$ **then**
        $\boldsymbol{y}_{init}^{(i+1)} \leftarrow \boldsymbol{y}^*(t_{i+1} - \Delta t_{slide})$
    else
        $\boldsymbol{y}_{init}^{(i+1)} \leftarrow \boldsymbol{y}^*(t_{i+1})$
    end if
end for
assemble $\boldsymbol{b}_c^*(t)$ on $[0, T]$ and remove the $\mathcal{T}_{shake}$ intervals before forming the steady-glide statistics

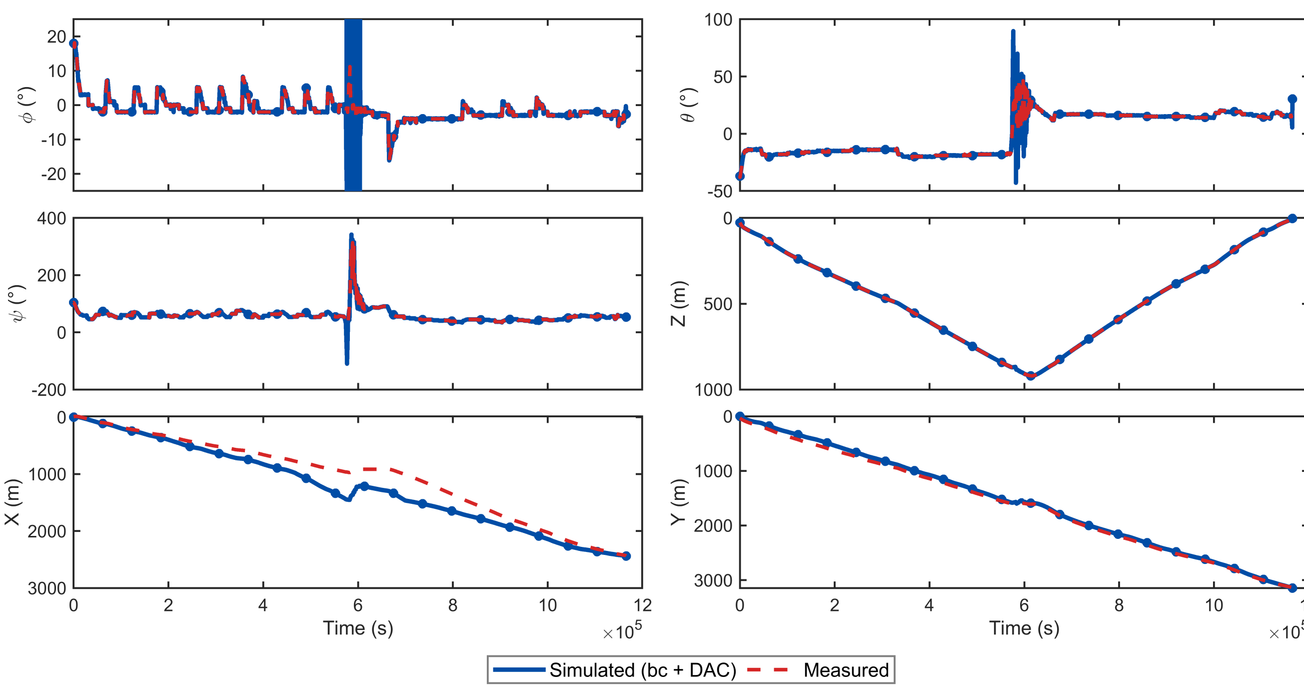

Figure 2: Comparison of motion state reconstruction versus measurements for Profile 18 using the optimized framework.

intentionally set to zero to assess the identification capability of the algorithm in the absence of prior knowledge. The solver adopts a segment duration of $T_{seg} = 30$ s and a sliding step of $\Delta t_{slide} = 10$ s to balance computational efficiency against tracking agility.

As illustrated in Fig. 2, the optimized attitude (ϕ, θ, ψ) and depth Z closely follow the measured records throughout the steady gliding phases, while the horizontal positions (X, Y), which lack a continuous measurement, are assessed qualitatively against the GPS-anchored reference. There the tracking RMSE is 2.4° in roll, 2.3° in pitch, and 2.15° in heading, with 0.31 m in depth. Fidelity degrades only over the brief attitude-adjustment intervals, where the errors rise to 16.2° in roll, 10.2° in pitch, and 11.1° in heading, with 1.20 m in depth, a factor of 3.8 to 6.8 above the steady-glide values. These intervals coincide with active operation of the internal actuators, and the degradation is most plausibly attributable to actuator-induced mechanical vibration that

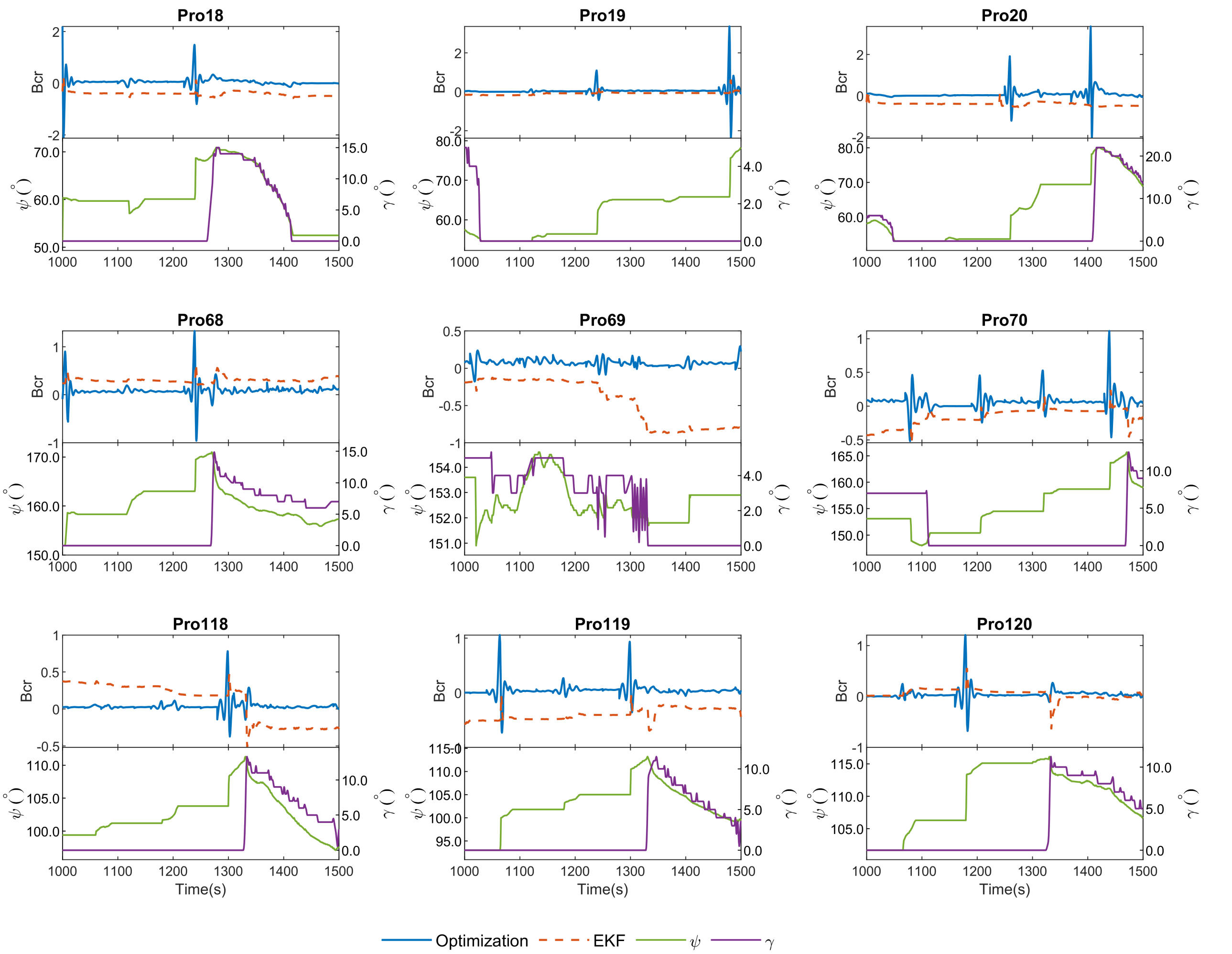

Figure 3: Yaw-rate disturbance B_{cr} identified by the adjoint-based dynamics inversion and the EKF across different motion profiles.

Table 1
Yaw rate coefficient β and R^2 across depth bins for each profile.

		Full Profile			Shallow			Mid-depth			Deep		
Profile	**Group**	Depth	β	R^2	Depth	β	R^2	Depth	β	R^2	Depth	β	R^2
Pro.18	Calm-A	206–811	5.62	0.998	206–395	6.65	0.986	395–586	3.62	0.962	586–811	4.98	0.974
Pro.19	Calm-A	200–821	5.72	0.991	200–410	6.97	0.981	410–635	5.13	0.967	635–821	4.58	0.969
Pro.20	Calm-A	204–819	5.41	0.982	204–432	5.68	0.983	432–645	4.24	0.950	645–819	4.42	0.952
Pro.68	Calm-B	209–803	5.23	0.994	209–423	4.51	0.957	423–581	4.35	0.976	581–803	3.51	0.914
Pro.69	Calm-B	194–808	5.10	0.979	194–425	4.50	0.939	425–608	4.05	0.959	608–808	4.80	0.971
Pro.70	Calm-B	199–809	4.64	0.975	199–410	4.19	0.958	410–587	3.53	0.942	587–809	4.14	0.968
Pro.118	Harsh	194–614	5.09	0.957	194–326	4.53	0.955	326–480	3.72	0.944	480–614	4.12	0.960
Pro.119	Harsh	193–607	5.02	0.963	193–312	4.34	0.954	312–471	3.99	0.956	471–607	4.05	0.959
Pro.120	Harsh	190–610	4.33	0.945	190–328	4.01	0.952	328–479	3.78	0.911	479–610	2.61	0.956

injects sensor noise departing from the smooth-dynamics assumption of the model. Such intervals occupy only a small fraction of the dive and are excluded from the statistical post-processing. Despite these local transient errors, the time-varying control vector $\boldsymbol{b}_c(t)$ successfully compensates for system uncertainties arising from unmodeled hydrodynamic coefficients and external disturbances throughout the majority of the profile.

For the horizontal channels, the dead-reckoning trajectory proposed by Zhou et al. [22] is adopted as a qualitative

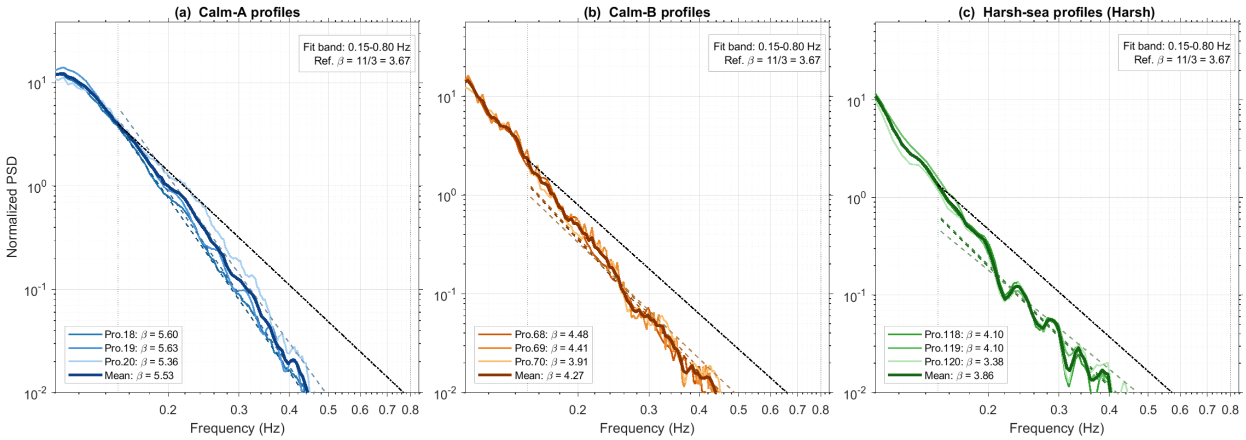

Figure 4: Normalized PSD of B_{cr} for (a) Calm-A, (b) Calm-B, and (c) Harsh groups. The dash-dotted line marks the theoretical reference $\beta_{\text{ref}} = 11/3$.

reference. As shown in the X and Y panels of Fig. 2, after applying the depth-averaged-current correction, the disturbance-compensated trajectory and the dead-reckoning reference are both anchored by the resurfacing GPS fix. This GPS anchoring is separate from the adjoint tracking problem itself, which imposes no horizontal terminal constraint and therefore retains the transversality condition $\lambda(T) = \mathbf{0}$. Intermediate discrepancies reflect the inherent differences between the two reconstruction approaches. The overall consistency in trend provides qualitative validation that the horizontal evolution of the simulated trajectory is reasonable. Combined with the high-fidelity matching in the attitude and depth channels, these results confirm the effectiveness of the proposed framework for reconstructing sensor-observable states.

Because the optimization is driven entirely by the onboard attitude and depth records, their accuracy sets a floor on the recovered fields. The sensor noise is calibrated against the records, with attitude quantized at the 0.1° compass resolution and depth carrying a 0.03 m standard deviation. Propagated through the full pipeline, this noise raises the identified yaw disturbance by at most 0.24 N·m and leaves the reconstructed through-water velocity uncertain by 2×10^{-4} m/s. Both values are far below the recovered signal. A systematic offset behaves differently from random noise. A heading offset is almost transparent to the identification and shifts every disturbance channel by a few $\times 10^{-3}$ N or N·m per degree, whereas a pitch offset is the dominant attitude sensitivity and maps into the axial force and pitch moment at 0.43 N and 0.11 N·m per degree on a steep dive. Either offset contributes a constant bias rather than a trend, so it shifts the baseline of the identified disturbance without distorting its temporal structure.

5.1.2. Computational Efficiency and Parameter Sensitivity

Practicality for routine post-processing first depends on the framework's computational cost. The adjoint inversion is an offline procedure whose cost is governed by the sliding-window structure. As reported in Table 2 for Profile 18, each 30 s window solves a compact non-convex subproblem that converges quickly, taking a median of 37 iterations and about 4.1 s on one core, with an interquartile range of 4 and a maximum of 69 under a first-order optimality tolerance of 10^{-3}. Because each window performs one forward and one adjoint integration of the 18-state augmented system, a full dive of about 389 windows completes in about 27 minutes, and the cost grows linearly with profile duration. For reference, the EKF baseline processes the same dive in about one minute as a single forward recursive pass, more than an order of magnitude faster. The per-window cost of 4.1 s is far below the 30 s of glider data each window spans, and the 27 minutes for a full dive is a small fraction of the dive duration of about 3.2 hours, so the computational budget is sufficient for the windowed inversion to keep pace with data acquisition. This establishes the feasibility of an incremental, receding-horizon implementation, notwithstanding the higher per-dive cost than the EKF. The lower block of the table compares the two methods on a common 600 s steady-glide segment, using the open-loop forward residual of each method's identified disturbance against the measured states. The adjoint reconstruction tracks attitude to within 0.28° and depth to 0.014 m, whereas the EKF reconstruction is markedly less accurate, reaching 3.34° in heading and 2.99 m in depth, because the causal filter smooths the sparse forcing that the adjoint resolves. The higher cost of the adjoint smoother is the price of this non-causal full-window reconstruction.

Reconstruction quality further depends on the window length and the slide step. Their effect is characterized on a twin experiment, in which the forward model synthesizes sensor data from a known synthetic disturbance that the same inversion then recovers, so that each setting is scored against ground truth. The window length was swept from 15 s to 90 s, and the representative reconstructions together with the resulting error metrics are shown in Fig. 5.

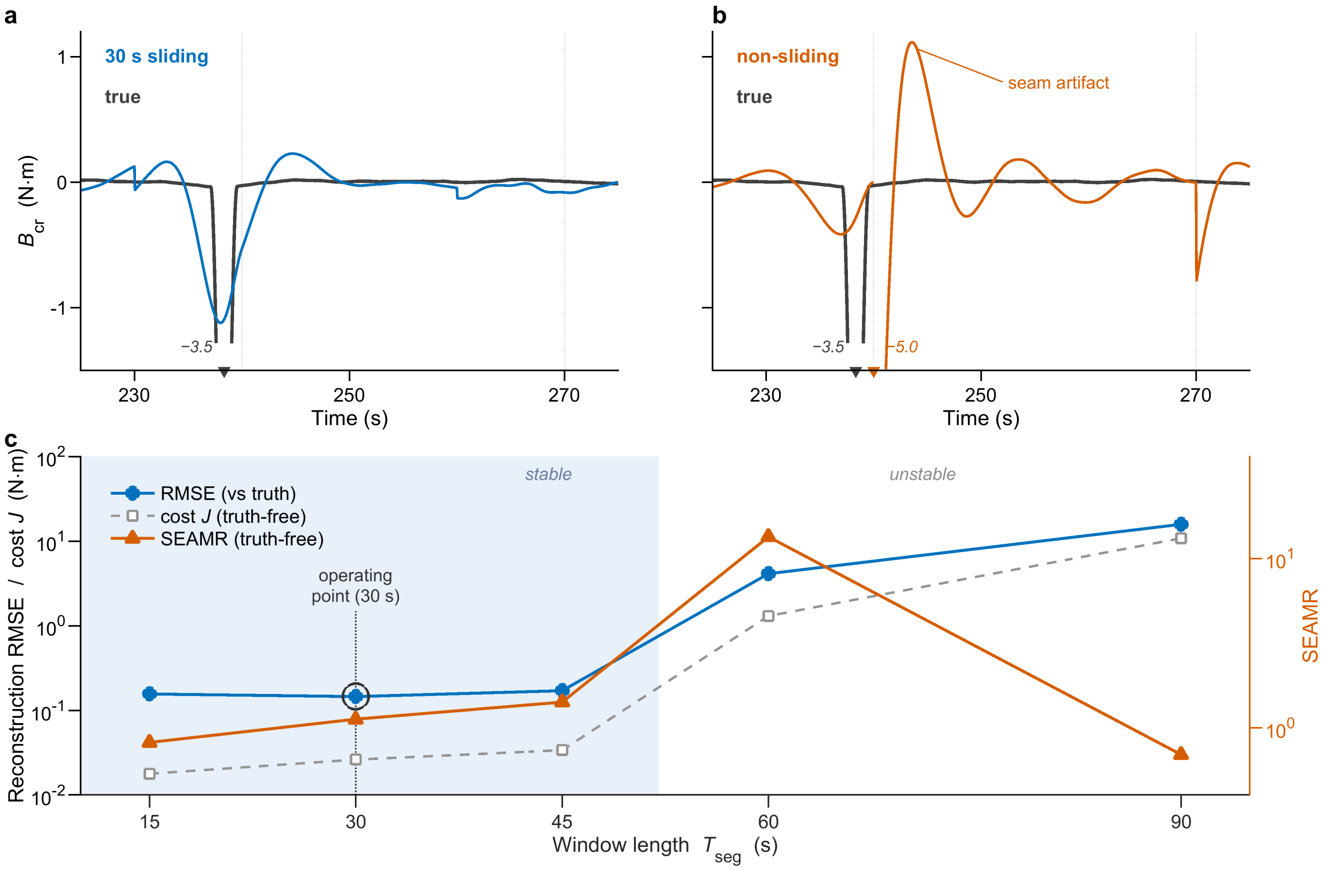

Figure 5: Sliding-window selection on the twin experiment. (a) 30 s sliding reconstruction against the truth, (b) non-sliding reconstruction with the seam artifact, and (c) reconstruction RMSE, optimizer cost J, and seam-artifact ratio (SEAMR) versus window length T_{seg}.

Table 2
Computational cost and open-loop state-tracking accuracy of the adjoint smoother and the EKF baseline. Profile 18, 600 s steady-glide segment, single core. Tracking RMSE is the open-loop reconstruction residual against the measured attitude and depth.

	Adjoint	EKF
Iterations per window	37	–
Time per window	4.1 s	–
Time per dive	26.6 min	0.85 min
RMSE, roll	0.057°	0.078°
RMSE, pitch	0.280°	1.015°
RMSE, heading	0.097°	3.340°
RMSE, depth	0.014 m	2.985 m

As shown in Fig. 5(a, b), the 30 s sliding window tracks the true disturbance closely, whereas the non-sliding segmentation injects a discontinuity at every boundary that appears as a seam artifact. Fig. 5(c) quantifies the trade-off: a 30 s window minimizes the reconstruction RMSE at about 0.15 N·m and keeps the seam-artifact ratio near one, shorter windows lose a small amount of fidelity, and beyond 45 s the per-window non-convex problem ceases to converge and produces high-amplitude artifacts. The non-sliding case attains a lower optimization cost yet raises the seam-artifact ratio above twenty, so the window must be selected by the reconstruction error against the truth rather than by the optimization cost. The cost threshold τ_c governs only the window handover, and the recovered disturbance is invariant as τ_c is swept from 0.05 to 3.2, so it acts as a safeguard for the rare poorly converged window rather than as a tuning parameter. These results fix the operating point at a 30 s window, a 10 s slide step, and $\tau_c = 0.2$.

5.2. Comparison of Adjoint-Based Inversion with EKF

To compare the disturbance-identification fidelity of the EKF and the adjoint method, three groups of consecutive profiles (Profiles 18–20, 68–70, 118–120) are selected at intervals of 50 profiles to cover a range of sea-state conditions. Profiles 18–20 and 68–70 correspond to relatively calm environments with small dead-reckoning deviations, while Profiles 118–120 correspond to a more energetic environment with noticeably larger deviations. Under identical physical parameters and initial conditions, the EKF prior and the adjoint-refined yaw-channel disturbance B_{cr} are extracted.

As shown in Fig. 3, the identification results obtained by the two methods exhibit distinctly different dynamic characteristics. The heading angle ψ and the rotation angle of the movable battery pack γ are plotted alongside B_{cr} as auxiliary state variables to elucidate the relationship between the actuation regime and the identified disturbance response.

Adjoint-based inversion reveals a regime-dependent structure closely tied to the actuation state. During steady-state gliding phases where $\gamma = 0$ and the internal roll actuator is inactive, the identified B_{cr} stays near zero for the majority of the interval, yet exhibits intermittent high-amplitude impulsive spikes that are temporally aligned with abrupt heading angle variations. The temporal correspondence between these impulsive signatures and the unactuated heading transients confirms that they originate from a physical mechanism rather than from numerical fitting artifacts. Since no active control input is present during these episodes, external hydrodynamic forcing represents the most probable source. During maneuvering phases where $\gamma \neq 0$, by contrast, the identified B_{cr} transitions to a sustained low-frequency oscillatory pattern with notably smaller amplitude. This qualitative shift points to a fundamentally different disturbance source. The persistent low-frequency component can be attributed to systematic modeling residuals, specifically the unmodeled coupling between internal actuation and hydrodynamic response together with parametric uncertainties in the dynamic model, both of which become significant only when the actuation mechanism is engaged. The coexistence of these two distinct disturbance regimes within a single profile indicates that the adjoint method possesses sufficient temporal resolution to separate transient impulsive events from persistent low-frequency model deficiencies.

By contrast, the EKF-identified B_{cr} exhibits a uniformly smooth and slowly varying profile regardless of the actuation state. During steady-state intervals with $\gamma = 0$, the EKF does not reproduce the impulsive signatures that the adjoint method associates with heading transients. Instead, it yields a gradually drifting signal whose attenuated amplitude obscures the transient disturbance structure. During maneuvering phases with $\gamma \neq 0$, the EKF output remains qualitatively indistinguishable from its steady-state behavior, leaving it unable to differentiate between the two physically distinct disturbance regimes described above. This limitation arises from the EKF's causal recursive architecture. Its Markovian state-transition assumption and Gaussian white-noise model act as an implicit low-pass filter that suppresses non-Gaussian impulsive events and spreads their energy across adjacent time steps. The genuine disturbance forcing is then absorbed into the measurement-noise estimate.

The two behaviors differ because the adjoint-based dynamics inversion, as a full-window optimization that uses both past and future information, removes the phase lag intrinsic to the EKF's causal recursion, providing a more faithful B_{cr} basis for the fine-scale current reconstruction and dead-reckoning correction that follow.

5.3. Power-Spectral Scaling and Consistency with Turbulence Theory

This subsection tests, in the frequency domain, whether the impulsive B_{cr} signatures originate from environmental turbulence by examining their spectral scaling and intermittency against established turbulence theory.

Grouped by depth-averaged current magnitude, the same nine profiles fall into Calm-A (Profiles 18–20), Calm-B (Profiles 68–70), and Harsh (Profiles 118–120). A fourth-order Butterworth high-pass filter with a 0.05 Hz cutoff removes the low-frequency modeling bias from B_{cr}, and the normalized power spectral density (PSD) of the residual is estimated by Welch's method. A power law $S(f) \propto f^{-\beta}$ is fitted over [0.15, 0.80] Hz to obtain the exponent β and the coefficient of determination R^2. Combining the Kolmogorov velocity spectrum $S_v \propto f^{-5/3}$ with the f^{-2} roll-off of the finite-size glider body gives a theoretical reference $\beta_{\mathrm{ref}} = 11/3 \approx 3.67$, about which the observed exponents scatter under real operating conditions. The group PSDs are shown in Fig. 4 and the depth-segment exponents are summarized in Table 1.

As shown in Fig. 4, all nine profiles follow a single power law over the resolved high-frequency band, with $R^2 > 0.95$ throughout. The spectral exponent decreases monotonically from the calm to the harsh groups, the group-averaged values being $\bar{\beta}_{\mathrm{Calm\text{-}A}} = 5.53$, $\bar{\beta}_{\mathrm{Calm\text{-}B}} = 4.27$, and $\bar{\beta}_{\mathrm{Harsh}} = 3.86$ with mean R^2 of 0.986, 0.971, and 0.956. The Harsh group lies closest to β_{ref}, consistent with stronger background currents driving more fully developed turbulence toward Kolmogorov inertial-subrange scaling while weaker currents yield steeper, less developed slopes.

Depth dependence is examined by splitting each profile into shallow, mid-depth, and deep segments of equal duration (Table 1). The Calm-B and Harsh segments stay within $\beta = 2.6$–4.8 with no depth trend, whereas the Calm-A shallow segments show markedly elevated exponents (5.68–6.97) that fall toward mid-depth (3.62–5.13) and deep (4.42–4.98). This shallow anomaly is attributable to the strong thermocline stratification, which suppresses vertical mixing and preferentially attenuates high-frequency fluctuations, steepening the apparent slope. Consistent with this, the mid-depth segment of Profile 18 recovers to $\beta = 3.62$ near β_{ref} once stratification weakens, while the deep segment of Profile 120 reaches the dataset minimum $\beta = 2.61$, consistent with enhanced near-bottom dissipation. All segment fits retain $R^2 > 0.91$.

Power-law scaling is only a consistency signature, since a linear stochastic process with a suitably colored spectrum can reproduce any β. The attribution is therefore tested against phase-sensitive intermittency statistics that such a process cannot imitate. For each profile, the increment flatness $F(\tau) = \langle \delta B_{cr}^4 \rangle / \langle \delta B_{cr}^2 \rangle^2$ and the extended-self-similarity (ESS) exponents ζ_p/ζ_3 [26] are compared with $N = 39$ IAAFT surrogates [27, 28] that preserve the power spectrum and amplitude distribution while destroying Fourier-phase coherence. The discriminating statistic, fixed

Table 3
Phase-sensitive intermittency statistics of the measured high-frequency B_{cr}, IAAFT surrogates, and the noise-only and model-error pipeline nulls. Entries are ranges over each ensemble, and the $\pm$ on ζ_6/ζ_3 is the standard deviation across the nine profiles.

	$F(1\,\mathrm{s})$	ζ_6/ζ_3	Kurtosis	Max amplitude (N·m)	β
IAAFT surrogates (linear stochastic)	30–221	1.85–1.98	preserved	preserved	$\approx$ preserved
Noise-only pipeline null (12 realizations)	18–87	0.85–1.98	13–43	≤ 0.24	2.4–5.8
Model-error pipeline null ($\pm$15%, 12 realizations)	16–52	0.46–1.99	14–40	≤ 0.48	2.4–5.2
Measured (nine profiles)	57–448	1.77 ± 0.05	30–187	0.36–2.98	3.4–5.6

a priori as $F(1\,\mathrm{s})$, is tested per profile by an exact one-sided rank test, giving $p = 1/(N+1) = 0.025$ when the measurement exceeds every surrogate. As shown in Fig. 6(a), the measured flatness grows toward small scales and exceeds its 39-surrogate envelope in all nine profiles. Because kurtosis is preserved by construction, the phase structure alone produces this discrimination. The ESS exponents (Fig. 6(b)) are anomalous and concave in all nine profiles, with $\zeta_6/\zeta_3 = 1.77 \pm 0.05$ against the She–Lévêque value of 1.78 [29], whereas the surrogates collapse toward the self-affine range 1.85–1.98.

Two pipeline-level nulls address the nonlinear artifact pathways that surrogates cannot probe. Synthetic observations were generated from the forward model with zero environmental disturbance, sampled at 1 Hz with the field-calibrated sensor model of Section 5.1, and inverted with the identical pipeline. The noise-only null used the nominal model, and the model-error null used a $\pm$15% perturbation of the viscous and added-mass coefficients. Each null comprised twelve realizations with independent seeds and coefficient draws. Both families produce steep power-law spectra with $\beta = 2.4$–5.8, fully covering the measured 3.4–5.6, so the spectral exponent alone carries no discriminating power. The phase-sensitive statistics separate them (Table 3). The null ζ_6/ζ_3 scatters over 0.46–1.99 across the twenty-four realizations, only three of which fall within $\pm$0.05 of the She–Lévêque value, and the null amplitudes never exceed 0.48 N·m, whereas the nine measured profiles, spanning two months and three sea states, cluster at $\zeta_6/\zeta_3 = 1.77 \pm 0.05$ with their twelve strongest events exceeding the null ceiling by up to six-fold. Were the per-profile exponent drawn from the null distribution, the joint probability of all nine lying in the measured cluster would be of order 10^{-8}. The discriminating signature therefore combines three features: nine consistent turbulence-valued exponents, amplitudes far above the artifact ceiling, and a passed per-profile surrogate test. No tested noise or model-error pathway reproduces this combination. These nulls span the stochastic-noise and constant-parameter-error pathways. Intermittent instrumental transients such as actuator vibration are handled separately. The $\mathcal{T}_{shake}$ rule excludes vibration-affected windows, and the impulsive events are confined to unactuated ($\gamma = 0$) intervals.

5.4. Depth-Resolved Ocean Current Inversion

From the glider's own attitude and depth records, the identified B_{cr} enables a depth-resolved reconstruction of the ocean current profile. The underlying physical premise is that a lateral current v_c modifies the body-frame velocity field, producing an incremental viscous yaw moment that the adjoint method captures as B_{cr}. At each time step, v_c is recovered by solving

$$M_z(u,\, v{-}v_c,\, w,\, p,\, q,\, r,\, \alpha) - M_z^{\mathrm{nom}} - (M_{f1} - M_{f2})\, u\, v_c = B_{cr,\mathrm{filt}} \tag{41}$$

where M_z^{nom} is the nominal yaw moment computed from the simulated velocity field in the absence of lateral current, M_{f1} and M_{f2} are the surge and sway added masses, and $B_{cr,\mathrm{filt}}$ is obtained by subtracting a 60 s moving-average baseline from the raw B_{cr} to remove slow mechanical-assembly bias. The solution for v_c is smoothed with a Savitzky–Golay filter, projected from the body frame to the NED inertial frame using the measured Euler angles, and superimposed on the depth-averaged current (DAC) from the GPS residual to yield the absolute current profile.

Fig. 7 presents the inversion result for Profile 68. The depth-resolved velocity profile (left panel) reveals pronounced current shear in the upper 200 m, with velocity fluctuations substantially exceeding those in the deep layer, consistent with wind-driven mixing and internal-wave modulation concentrated near the surface. Below approximately 400 m, both components converge toward the DAC baselines ($\mathrm{DAC}_N = -0.112$ m/s, $\mathrm{DAC}_E = -0.023$ m/s), indicating that the deep current field is dominated by the mean drift with limited vertical shear. The trajectory view (right panel) shows that the reconstructed shear vectors capture the depth-dependent lateral deflection of the glider path. Because the depth-averaged correction is fixed by the GPS residual, the simulated track closing on the GPS reference is a consistency check rather than an independent validation. These results demonstrate the feasibility of retrieving depth-stratified current information from standard glider attitude and depth measurements by coupling the adjoint-identified disturbance with the moment-inversion model. The depth-averaged baseline and its uncertainty are assessed against independent reanalyses in Section 5.5.

5.5. Cross-Validation against Ocean Reanalyses

For cross-validation, the recovered current is compared against two independent eddy-resolving reanalyses, HYCOM GOFS 3.1 [30] and GLORYS12 [31], both of 1/12° resolution and sampled at the time and location of each

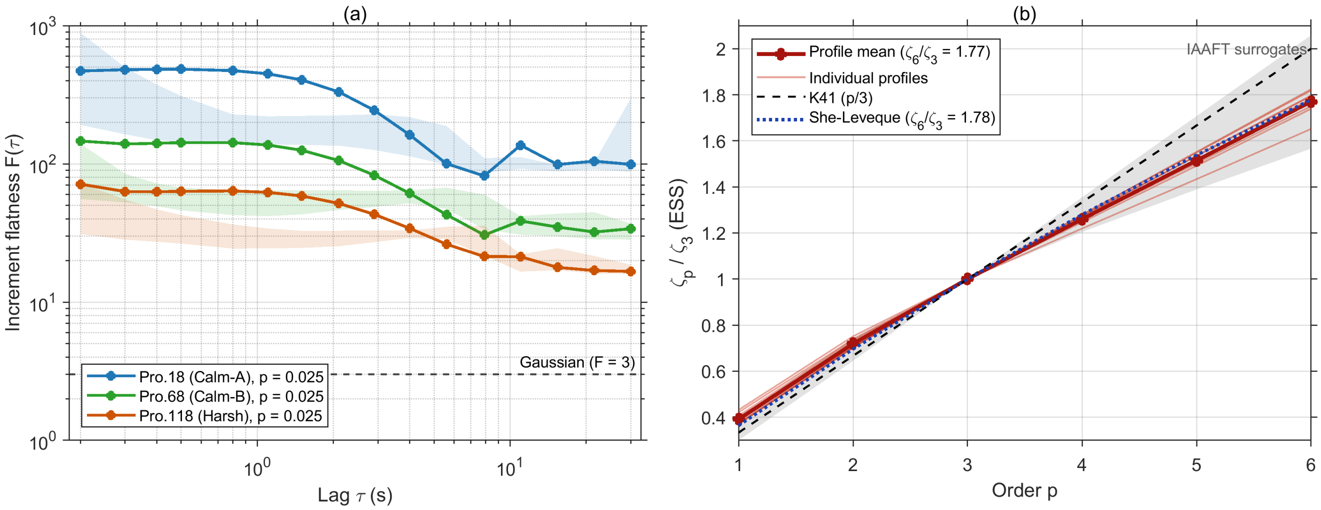

Figure 6: Falsifiability tests of the turbulence attribution. (a) increment flatness $F(\tau)$ of the high-frequency B_{cr} against its 39-surrogate envelope, and (b) ESS exponents ζ_p/ζ_3 against the surrogate envelope, the Kolmogorov (K41) scaling $p/3$, and the She–Lévêque model.

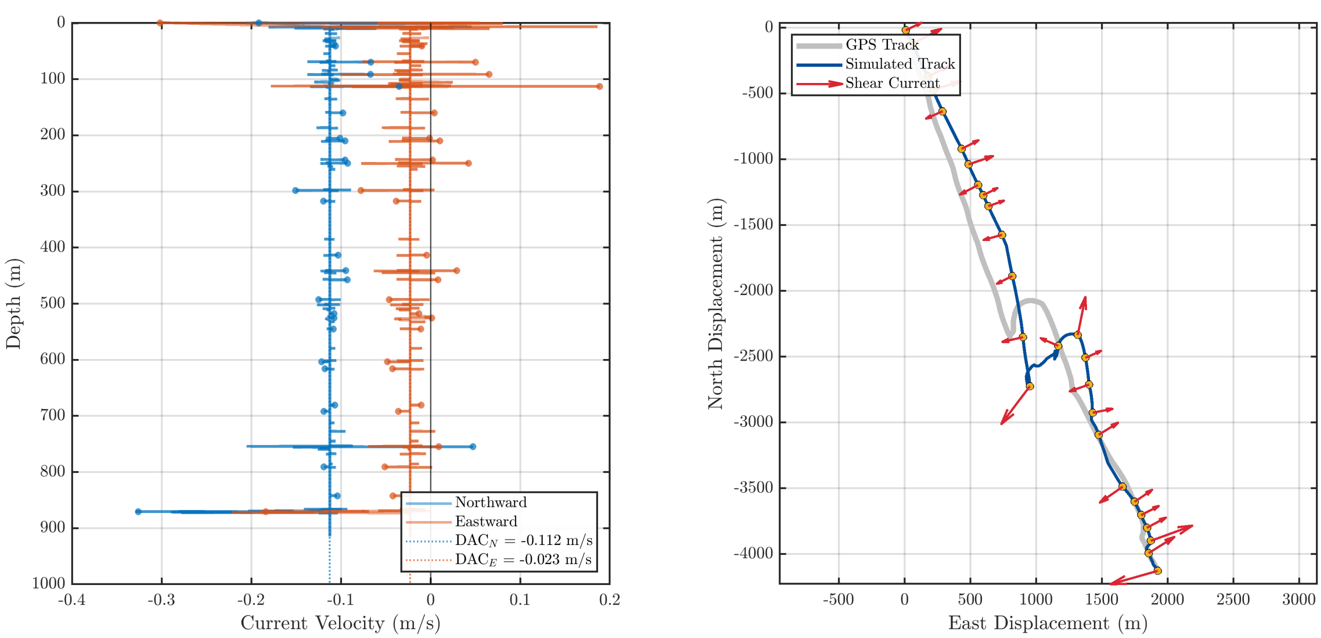

Figure 7: Depth-resolved current inversion for Profile 68. Left: absolute current velocity profile with DAC baselines. Right: horizontal trajectory with shear-current vectors.

profile. Only the depth-averaged current, the DAC, enters this comparison. The DAC is constrained directly by the surfacing GPS displacement and sets the absolute baseline of Fig. 7, whereas the depth-resolved shear inferred from B_{cr} varies on vertical and temporal scales finer than the reanalysis grid, so a pointwise comparison with the gridded products is not meaningful. The adjoint DAC, the glide-angle DAC, and the two reanalyses are compared for nine profiles evenly sampled over mission days 2–65 in Fig. 8 and Table 4.

All four estimates have depth-averaged speeds of 0.04–0.42 m/s, consistent with the spring circulation of the northern South China Sea, and the adjoint and conventional glide-angle directions [32] agree to a median of about 8°. Measured against the uncertainty ellipses, HYCOM lies within 2σ of the adjoint DAC on five of the nine profiles and within 3σ on six, and GLORYS12 within 2σ on two and within 3σ on six. On Profiles 329 and 430 the adjoint and glide-angle estimates agree closely, yet both reanalyses lie at 3.6σ–5.0σ, and across the nine profiles the two reanalyses themselves differ by 0.2°–127° in direction, with a mutual vector RMSD of 0.11 m/s. These residual distances therefore reflect the spread among the reanalyses rather than an error of the

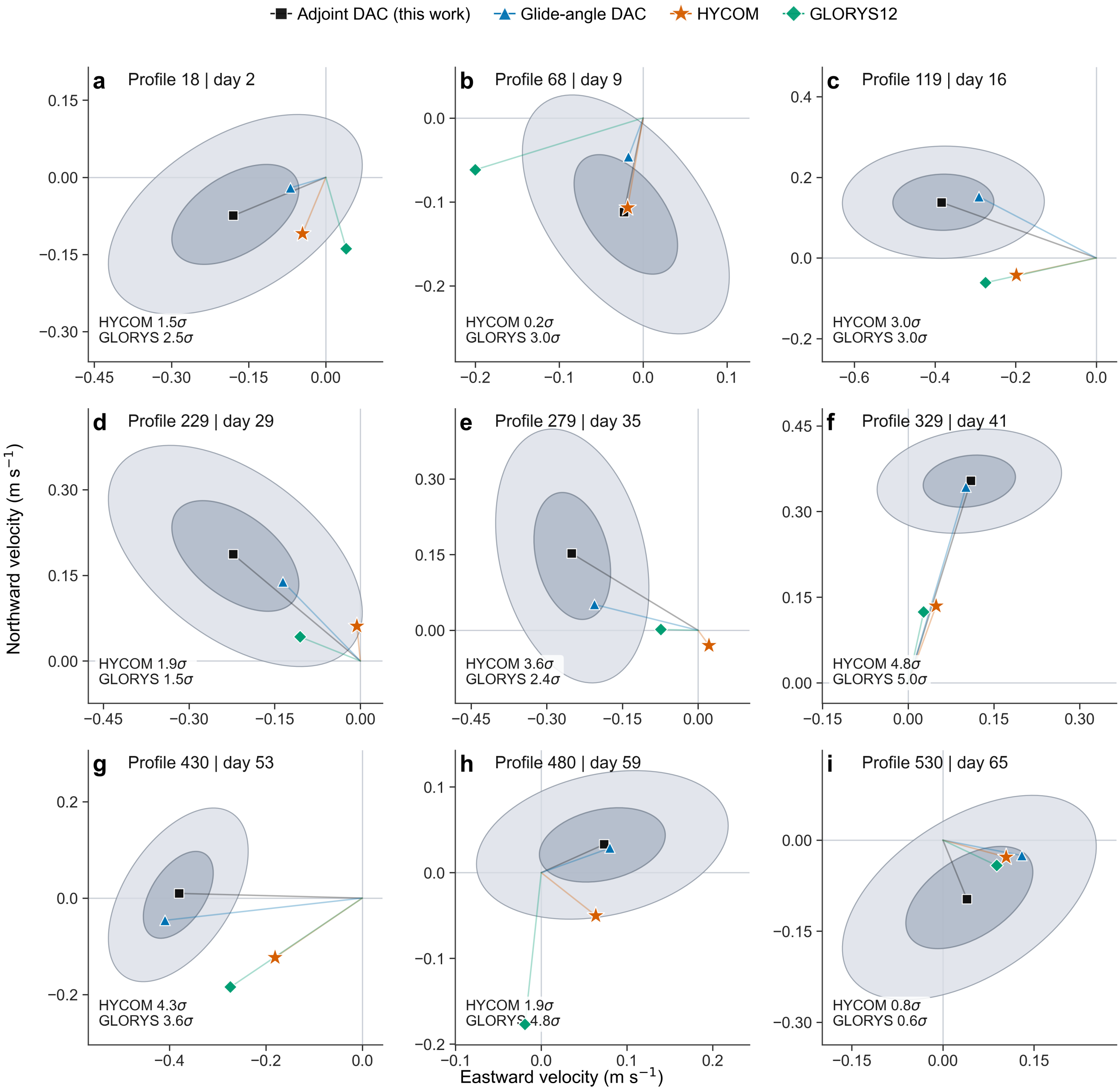

Figure 8: Depth-averaged current cross-comparison for nine profiles evenly sampled across the mission, showing the adjoint DAC (black square) with its 1σ and 2σ ellipses, the glide-angle DAC (blue triangle), HYCOM (red star), and GLORYS12 (green diamond). Annotations give each reanalysis's distance from the ellipses in σ.

inversion, and in this eddy-rich region no single gridded product can serve as a profile-by-profile reference.

The DAC is the residual between the GPS displacement and the glider's modeled through-water self-motion, so it is sensitive to that self-motion, and the adjoint DAC consequently sits on the high-magnitude side of the spread on the mid-mission profiles. The error in recovering this self-motion is measured by the twin experiments, and two effects enter the budget. The first is the mechanical vibration injected by internal actuation during the brief attitude-adjustment intervals. These intervals occupy only 6.3–8.4% of each dive, yet the through-water displacement they contribute amounts to 0.03–0.05 m/s, or 10–44% of the profile DAC, so they are detected from the actuation channel and excluded from the reported estimates. The second is the residual error that remains even with a perfect model, where the recovered displacement keeps a velocity error of 0.05–0.06 m/s. This error is set by a spurious axial offset of about -0.5 N, which grows to between -0.4 and -0.75 N under a $\pm 15\%$ coefficient perturbation, whereas sensor noise alone leaves only about 2×10^{-4} m/s. The ellipses of Fig. 8 combine three terms, this axial weak observability, a conservative 26% relative magnitude uncertainty, and an 8°

Table 4
Depth-averaged current speed $|\mathbf{V}|$ (m/s) and direction θ_c for the nine profiles of Fig. 8, from the adjoint inversion, the glide-angle method, and the HYCOM and GLORYS12 reanalyses. The last two columns give each reanalysis's distance from the uncertainty ellipses in σ.

		Adjoint		**Glide-angle**		**HYCOM**		**GLORYS12**		**Dist. (σ)**	
Pro	**Day**	$\|\mathbf{V}\|$	θ_c	$\|\mathbf{V}\|$	θ_c	$\|\mathbf{V}\|$	θ_c	$\|\mathbf{V}\|$	θ_c	HYCOM	GLORYS
18	2	0.195	248	0.072	254	0.118	203	0.144	164	1.5	2.5
68	9	0.115	191	0.049	201	0.108	190	0.209	253	0.2	3.0
119	16	0.408	290	0.328	298	0.202	258	0.281	257	3.0	3.0
229	29	0.291	310	0.194	316	0.062	354	0.113	292	1.9	1.5
279	35	0.293	301	0.212	284	0.037	144	0.074	271	3.6	2.4
329	41	0.370	17	0.357	16	0.143	20	0.127	12	4.8	5.0
430	53	0.380	271	0.412	264	0.219	236	0.330	236	4.3	3.6
480	59	0.081	66	0.085	70	0.081	128	0.178	186	1.9	4.8
530	65	0.105	158	0.132	101	0.108	105	0.098	115	0.8	0.6

heading uncertainty. The 26% bound covers the $\sim$ 18% RMS spread between the adjoint and glide-angle self-motion estimates. Where the reanalyses fall within these ellipses, they corroborate the retrieved DAC as an oceanographically plausible absolute offset.

A recoverability floor for the depth-resolved shear follows from the same twin experiments. An impulsive yaw event is recovered at the correct instant once its amplitude exceeds roughly 25–40 times the identification noise floor of 0.4–0.7 N·m. The glider's directional-stability filtering attenuates the amplitude three- to five-fold, so the retrieved shear magnitudes are reported as lower bounds. Perturbing the moment-inversion coefficients by $\pm$15% over 300 draws varies the shear amplitude by about 30% across the ensemble on the significant samples, because the viscous and Munk yaw moments nearly cancel. The absolute current magnitude changes by under 1.5%, since it stays anchored by the GPS-constrained depth-mean. The depth-resolved shear is therefore a sub-grid structure of bounded amplitude, while the depth-mean it sits on stays anchored by the GPS constraint and cross-checked against the reanalyses.

5.6. Long-Term Hydrodynamic Parameter Drift

Beyond a single profile, the adjoint-identified disturbance parameters can be tracked across the full mission to test whether the glider's effective hydrodynamics change over time. The analysis uses an evenly sampled grid of eleven epochs spaced every fifty profiles, from Pro. 18 to Pro. 530. Each epoch is a consecutive triple, which gives $n = 33$ profiles over mission days 2–65, plotted against the true elapsed flight time recorded on board. For each profile, every disturbance component is summarized by the median of all steady-gliding samples within the common 150–500 m depth band, with the attitude-adjustment intervals excluded. The diving and climbing phases are treated separately, so that any angle-of-attack-dependent asymmetric component is retained rather than cancelled by a dive-climb average. Each profile triple also furnishes a within-epoch repeatability estimate, the identification noise floor. Monotonic trends are quantified non-parametrically with the Mann–Kendall test and the Theil–Sen slope with a block-bootstrap 95% confidence interval rather than a linear R^2. A component is taken as primary evidence only where the two estimators agree, namely where the Mann–Kendall $p < 0.05$ and the slope confidence interval excludes zero. The evolution of all six components is shown in Fig. 9, with the corresponding statistics in Table 5.

In the top row of Fig. 9, the axial disturbance B_{cu}, a direct proxy for parasitic drag, decreases monotonically in both phases, with Mann–Kendall $p = 2.3 \times 10^{-3}$ on the diving phase and 1.8×10^{-5} on the climbing phase, amounting to a -1.39 N or -39% change over the mission in the climbing phase. Its Theil–Sen confidence interval excludes zero, and it is the most robust single indicator. The heave disturbance B_{cw} and the pitch moment B_{cq} show a significant monotonic trend on the climbing phase, with Mann–Kendall $p = 0.039$ and 0.049 and mission drifts $\Delta = -4.41$ N and -1.69 N·m, magnitudes that reproduce the -4.55 N and -1.87 N·m of the preliminary analysis. Their Theil–Sen intervals still include zero, however, and neither is significant on the diving phase, so by the agreement criterion only B_{cu} qualifies as primary evidence and the climbing-phase B_{cw} and B_{cq} remain supporting. The significant drift is thus confined to the longitudinal plane, and it is markedly asymmetric between the two phases, the heave and pitch signals being carried almost entirely by the climbing phase, which indicates a forcing that depends on the sign of the angle of attack.

In the bottom row, the sway force B_{cv} shows no significant trend on either phase, and the largest lateral moment drift, 0.082 N·m in B_{cp}, is one to two orders below the largest longitudinal moment drift of 1.69 N·m. The roll moment B_{cp} and the yaw moment B_{cr} do reach formal statistical significance in Table 5, which is unsurprising at this sample size, but their magnitudes are negligible and lie one to two orders below the longitudinal signal. The slow B_{cr} baseline is in any case removed by the moving-average subtraction used in the current inversion. The lateral plane thus carries no comparable drift, and this near-total confinement to the

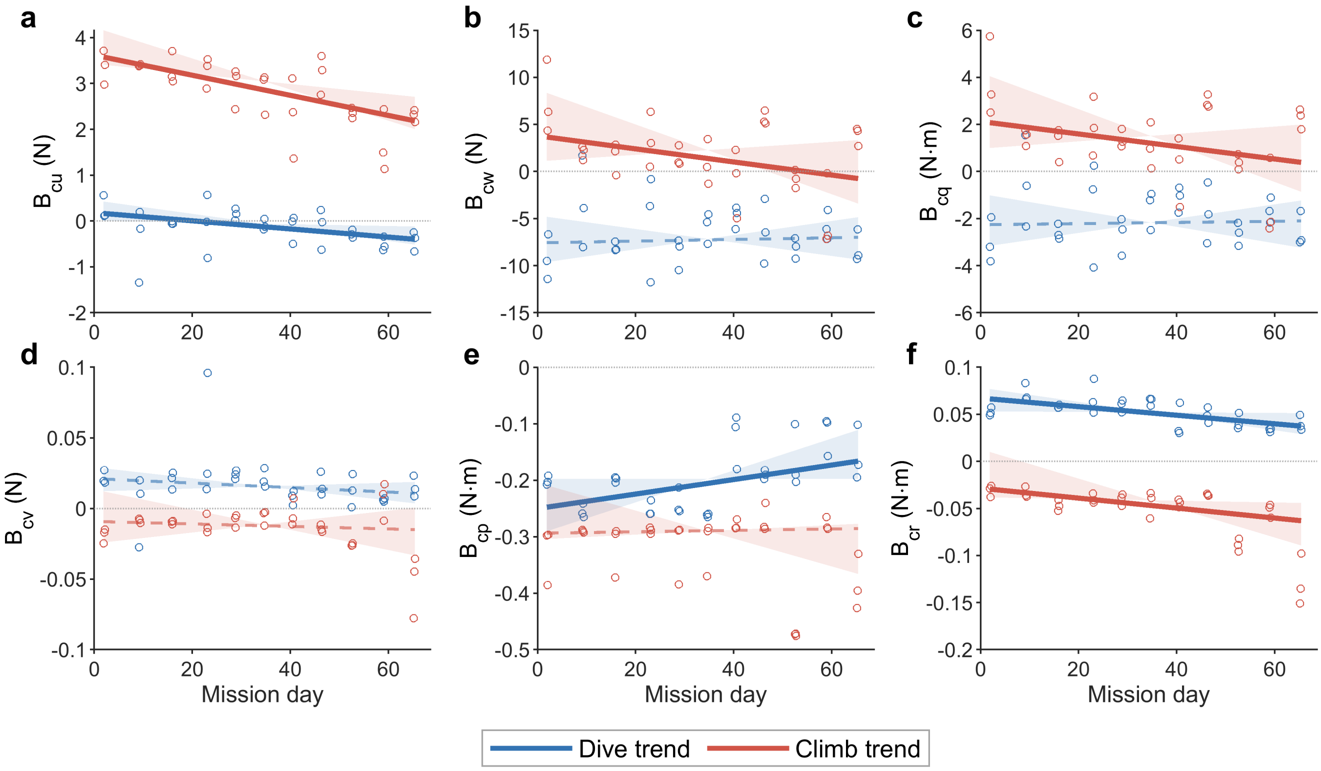

Figure 9: Long-term drift of the six lumped-disturbance components over the 65-day record, with the diving (blue) and climbing (red) phases shown separately. Solid lines mark a significant monotonic trend (Mann–Kendall $p < 0.05$) and dashed lines non-significant phases. The top row is the longitudinal plane and the bottom row the lateral plane.

Table 5

Monotonic-trend statistics of the six lumped-disturbance components over the full record ($n = 33$, mission days 2–65), with the diving and climbing phases analyzed separately. Columns give the Mann–Kendall τ and p, the Theil–Sen slope per day with 95% confidence interval, the mission drift Δ, and the ratio $|\Delta|/\sigma_f$ to the noise floor. The Tier column grades each component as Primary, Supp., or negligible.

Comp.	Phase	MK τ	MK p	Theil–Sen slope d^{-1} [95% CI]	Δ_{mission}	$\lvert\Delta\rvert/\sigma_f$	Tier
B_{cu} (N)	Dive	−0.38	2.3×10^{-3}	−0.0089 [−0.0148, −0.0019]	−0.56	2.6	Primary
	Climb	−0.53	1.8×10^{-5}	−0.0219 [−0.0339, −0.0110]	−1.39 (−39%)	3.8	Primary
B_{cw} (N)	Dive	+0.04	0.75	+0.0088 [−0.072, +0.075]	+0.56	0.3	–
	Climb	−0.25	0.039	−0.070 [−0.185, +0.035]	−4.41	2.6	Supp.
B_{cq} (N·m)	Dive	+0.02	0.89	+0.0025 [−0.035, +0.030]	+0.16	0.2	–
	Climb	−0.24	0.049	−0.027 [−0.077, +0.016]	−1.69	2.3	Supp.
B_{cv} (N)	Dive	−0.22	0.070	−0.0002 [−0.0004, +0.0001]	−0.010	1.5	–
	Climb	−0.08	0.53	−0.0001 [−0.0007, +0.0004]	−0.006	1.1	–
B_{cp} (N·m)	Dive	+0.36	3.8×10^{-3}	+0.0013 [0.000, +0.0028]	+0.082	6.0	(neg.)
	Climb	+0.11	0.38	+0.0001 [−0.0025, +0.0004]	+0.008	0.3	–
B_{cr} (N·m)	Dive	−0.41	8.6×10^{-4}	−0.0005 [−0.0008, 0.000]	−0.029	3.6	(neg.)
	Climb	−0.48	1.0×10^{-4}	−0.0005 [−0.0016, −0.0001]	−0.034	5.4	(neg.)

longitudinal plane indicates that the underlying process preserves the hull's lateral symmetry. A sensor bias or a numerical artifact would contaminate all six channels, whereas the observed drift leaves both lateral force and moment channels far smaller than their longitudinal counterparts.

The significant climbing-phase longitudinal drifts exceed the within-epoch identification noise floor by factors of 2–4 in Table 5, so they are not short-term identification scatter. A ±15% Monte-Carlo propagation on the hydrodynamic coefficients leaves the sign of every longitudinal slope unchanged in all 300 draws in Table 6, since a constant parameter error shifts the disturbance offset but not its trend. An entirely adjoint-independent degradation proxy, the forward-model longitudinal RMSE of Fig. 1(c),

Table 6
Robustness of the longitudinal-plane drift. The top rows give Monte-Carlo Theil–Sen slopes under a ±15% coefficient perturbation. The bottom rows give the adjoint-independent forward-model RMSE cross-check of Fig. 1(c).

Parameter MC: trend slope (d^{-1})			
Comp.	**Phase**	**Nominal**	**MC 95% CI**
B_{cu}	Dive	−0.016	[−0.019, −0.012]
B_{cu}	Climb	−0.019	[−0.024, −0.014]
B_{cw}	Climb	−0.028	[−0.040, −0.020]
B_{cq}	Climb	−0.013	[−0.018, −0.006]
Independent forward-model RMSE corroboration			
Monotonic rise: Mann–Kendall $p = 7.5\times10^{-6}$ (+66%, 0.048 → 0.080)			
Spearman(RMSE, day) = +0.69; Spearman(RMSE, $\|B_{cu}\|_{\text{climb}}$) = +0.75			

rises monotonically over the mission and correlates with the identified drag drift, again in Table 6. A drifting attitude calibration is ruled out as well, because a constant pitch offset would shift the axial channel in opposite directions on the diving and climbing phases, whereas the observed drag drift keeps the same sign on both. These independent checks corroborate the drift as a physical change in the glider's hydrodynamics, one that is significant, robust to parameter error, confined to the longitudinal plane, and asymmetric in the angle of attack. Such behavior is consistent with a gradual change in the glider's external hydrodynamic shape. The most plausible cause is the progressive biofouling and surface roughening that accumulate over a long deployment, which thicken the boundary layer and raise the form drag without breaking the hull's lateral symmetry. As the study is observational, other contributions cannot be excluded. A slowly varying buoyancy-engine effect, such as trapped air in the oil circuit, may add to the B_{cw} drift. Subject to these caveats, the identified drift can be used to monitor glider health and hull fouling from standard onboard sensor data alone.

6. Methodological Position and Limitations

Methodologically, the framework shares its adjoint machinery with variational data assimilation [33, 34] but inverts the glider rather than the ocean. The forward model is the glider's nonlinear 6-DOF dynamics, the observations are the platform's own attitude and depth records, and the inferred quantity is the lumped disturbance acting on it, so neither an ocean-model background nor a prescribed background-error covariance is required. Within the estimator family the method is a windowed variational smoother rather than a recursive observer. This non-causal, full-window formulation uses both past and future records and imposes no quadratic penalty that would shrink the disturbance toward zero, so it reconstructs the sparse, heavy-tailed impulses that a causal EKF redistributes across neighboring steps.

The principal limitation of the framework is one of accuracy rather than data availability. The windowed inversion runs on any segment whose onboard records are complete, at a computational cost that grows linearly with segment duration, but the records constrain the disturbance only incompletely. The fundamental cause is incomplete state observation. The onboard sensors record only attitude and depth, the velocities are never measured directly, and the horizontal position is known only at surfacing through the GPS fix. The through-water self-motion is therefore weakly observable, and this under-determination is the dominant source of uncertainty in the recovered depth-averaged current. Lateral currents reach the records only after being low-pass filtered by the glider's directional-stability dynamics, so the retrieved shear magnitudes are reported conservatively as lower bounds. In the absence of a co-deployed velocity reference, the inferred quantities are corroborated by cross-checking several independent lines of evidence. This standard is stronger than agreement with any single measured product. Within a segment, accuracy is reduced only during the brief actuation intervals, where mechanical vibration departs from the smooth-dynamics assumption. These intervals are detected from the actuation channel and excluded from the statistical post-processing. The remaining bound is the fidelity of the forward model, which the lumped disturbance absorbs but does not eliminate. The framework is most effective where the environmental forcing is energetic and intermittent. It is least effective in weak-current, strongly stratified conditions, where the signal approaches the identification noise floor. These bounds concern the absolute magnitude of the externally unconstrained components. The temporal structure, spectral and intermittency signatures, depth-resolved shear pattern, and long-term parameter drift on which the main conclusions rest remain robust to them.

7. Conclusion

This paper presented an adjoint-based dynamics inversion framework that reformulates disturbance identification as a full-window optimal-tracking problem through a six-dimensional lumped disturbance vector. Validation on operational sea-trial data demonstrated that the framework reconstructs regime-dependent disturbance signatures at a temporal resolution the EKF baseline does not reach. The identified high-frequency component follows the power-law spectral scaling predicted by Kolmogorov turbulence combined with rigid-body inertial filtering, with She–Lévêque intermittent structure-function scaling that survives the surrogate-data, noise-only, and model-error falsification tests. Twin experiments reproduce the self-motion under-determination as a structural property of the inversion and locate the recoverability floor of impulsive events. Coupling the characterized disturbance with a viscous-moment inversion model enabled depth-resolved current retrieval without acoustic Doppler hardware. The depth-averaged component was evaluated against the glide-angle method and two independent reanalyses, and the residual differences were traced to the under-determination of the glider self-motion. Long-term parameter tracking revealed a statistically significant, parameter-robust monotonic hydrodynamic drift most plausibly attributable to progressive biofouling. The framework serves as a virtual sensor for multi-dimensional environmental sensing and glider health assessment using only standard onboard measurements. It transfers in principle to any buoyancy-driven glider with a 6-DOF flight model, standard attitude and depth records, and a surfacing GPS fix. Porting to a new platform requires only substituting the hull-specific hydrodynamic and added-mass coefficients. Future work will focus on adapting the formulation to a receding-horizon architecture for near-real-time onboard estimation, and on cross-validation across additional platforms and sea states with co-deployed acoustic Doppler or microstructure instruments.

8. Acknowledgements

This work is jointly supported by the National Key R&D Program of China, the National Natural Science Foundation of China under Grant No. 62373278, the National Key R&D Program of China No. 2024YFA1012803, the basic research fund of Tianjin University No. 2025XJ21-0010, and the National Natural Science Foundation of China No. 12271400 (L. Wei and Y. Zhang).

References

[1] L. Liu, S. Peng, J. Wang, R. X. Huang, Retrieving density and velocity fields of the ocean's interior from surface data, J. Geophys. Res. Oceans 119 (2014) 8512–8529. https://doi.org/10.1002/2014JC010221.

[2] Y. C. Pan, Z. Dai, H. Ma, J. Zheng, J. Leng, C. Xie, Y. Yuan, W. Yang, Y. Yalikun, X. Song, et al., Self-powered and speed-adjustable sensor for abyssal ocean current measurements based on triboelectric nanogenerators, Nat. Commun. 15 (2024) 6133. https://doi.org/10.1038/s41467-024-50581-w.

[3] C. Zhou, H. Xu, X. Xiao, W. Zhao, J. Yang, Q. Yang, H. Jiang, Q. Xie, T. Long, T. Wang, et al., Intense abyssal flow through the Yap-Mariana junction in the Western North Pacific, Geophys. Res. Lett. 49 (2022) e2021GL096530. https://doi.org/10.1029/2021GL096530.

[4] J. Wang, F. Wang, Y. Lu, Q. Ma, L. J. Pratt, Z. Zhang, Pathways, volume transport, and seasonal variability of the lower deep limb of the Pacific meridional overturning circulation at the Yap-Mariana junction, Front. Mar. Sci. 8 (2021) 672199. https://doi.org/10.3389/fmars.2021.672199.

[5] C. C. Finlay, J. Velímskỳ, C. Kloss, R. M. Blangsbøll, Satellite monitoring of long period ocean-induced magnetic field variations, Philos. Trans. R. Soc. A 382 (2024) 20240077. https://doi.org/10.1098/rsta.2024.0077.

[6] Y. Wang, Y. Zhang, L. Wang, Z. Li, Z. Ma, C. Zhang, L. Chang, J. Wang, W. Ma, Modeling and performance analysis of underwater gliders based on the virtual prototype technology, Ocean Eng. 281 (2023) 114763. https://doi.org/10.1016/j.oceaneng.2023.114763.

[7] S. Fan, P. Yuan, J. Feng, H. Huang, S. Hu, Z. Zhao, Y. Zhu, K. Wang, Observing typhoon-driven upper ocean dynamics in the South China Sea using a virtual mooring underwater glider array: methods and analysis, J. Ocean Eng. Sci. 11 (2026) 33–57. https://doi.org/10.1016/j.joes.2025.09.003.

[8] M. Yang, Y. Wang, C. Wang, Y. Liang, S. Yang, L. Wang, S. Wang, Digital twin-driven industrialization development of underwater gliders, IEEE Trans. Ind. Inform. 19 (2023) 9680–9690. https://doi.org/10.1109/TII.2023.3233972.

[9] T. Wang, R. Juan, M. Luo, J. Chen, Y. Li, Y. Zhou, Z. Gao, Event-triggered model predictive control for trajectory tracking of underwater gliders in currents, Ocean Eng. 343 (2026) 123341. https://doi.org/10.1016/j.oceaneng.2025.123341.

[10] C. Jiang, J. Li, W. Xu, The use of underwater gliders as acoustic sensing platforms, Appl. Sci. 9 (2019) 4839. https://doi.org/10.3390/app9224839.

[11] E. Anderlini, D. A. Real-Arce, T. Morales, C. Barrera, J. J. Hernandez-Brito, A. B. Phillips, G. Thomas, A marine growth detection system for underwater gliders, IEEE J. Ocean. Eng. 46 (2021) 1099–1113. https://doi.org/10.1109/JOE.2021.3066373.

[12] B. Qiu, M. Wang, H. Li, L. Ma, X. Li, Z. Zhu, F. Zhou, Development of hybrid neural network and current forecasting model based dead reckoning method for accurate prediction of underwater glider position, Ocean Eng. 285 (2023) 115486. https://doi.org/10.1016/j.oceaneng.2023.115486.

[13] K. Course, P. B. Nair, State estimation of a physical system with unknown governing equations, Nature 622 (2023) 261–267. https://doi.org/10.1038/s41586-023-06574-8.

[14] N. E. Leonard, J. G. Graver, Model-based feedback control of autonomous underwater gliders, IEEE J. Ocean. Eng. 26 (2002) 633–645. https://doi.org/10.1109/48.972106.

[15] S. Fan, C. A. Woolsey, Dynamics of underwater gliders in currents, Ocean Eng. 84 (2014) 249–258. https://doi.org/10.1016/j.oceaneng.2014.03.024.

[16] Y. Wang, W. Han, W. Niu, M. Yang, Y. Teng, S. Yang, Dynamic modeling, motion analysis and fault diagnosis of underwater gliders with the loss of one wing, Appl. Math. Model. 123 (2023) 546–565. https://doi.org/10.1016/j.apm.2023.07.020.

[17] H. Wu, J. Ding, W. Niu, M. Liao, Y. Song, L. Tan, S. Yan, Combination optimization method for motion trajectory of morphing underwater gliders balancing energy efficiency and motion accuracy, Ocean Eng. 329 (2025) 121154. https://doi.org/10.1016/j.oceaneng.2025.121154.

[18] W. Zang, B. Wang, H. Zhang, D. Song, T. Guo, Angle of attack enhanced trajectory prediction for underwater gliders based on fuzzy-fusion of inference and dynamics, IEEE Trans. Fuzzy Syst. 34 (2026) 1–13. https://doi.org/10.1109/TFUZZ.2025.3618155.

[19] X. Yang, X. Liu, S. Yin, Robust identification of nonlinear systems with missing observations: The case of state-space model structure, IEEE Trans. Ind. Inform. 15 (2018) 2763–2774. https://doi.org/10.1109/TII.2018.2871194.

[20] X. Mao, J. He, Unidentifiability of system dynamics: Conditions and controller design, IEEE Trans. Autom. Control 70 (2025) 1380–1387. https://doi.org/10.1109/TAC.2024.3469392.

[21] H. Abdulsamad, P. Nickl, P. Klink, J. Peters, Variational hierarchical mixtures for probabilistic learning of inverse dynamics, IEEE Trans. Pattern Anal. Mach. Intell. 46 (2023) 1950–1963. https://doi.org/10.1109/TPAMI.2023.3314670.

[22] H. Zhou, J. Cao, J. Fu, C. Liu, Z. Wei, C. Yu, Z. Zeng, B. Yao, L. Lian, Dynamic modeling and motion control of a novel conceptual multi-modal underwater vehicle for autonomous sampling, Ocean Eng. 240 (2021) 109917. https://doi.org/10.1016/j.oceaneng.2021.109917.

[23] M. Yang, Y. Wang, X. Zhang, Y. Liang, C. Wang, Parameterized dynamic modeling and spiral motion pattern analysis for underwater gliders, IEEE J. Ocean. Eng. 48 (2023) 112–126. https://doi.org/10.1109/JOE.2022.3181896.

[24] J. Cao, J. Cao, B. Yao, L. Lian, Three dimensional model, hydrodynamics analysis and motion simulation of an underwater glider, in: OCEANS 2015-Genova, IEEE, 2015, pp. 1–8. https://doi.org/10.1109/OCEANS-Genova.2015.7271365.

[25] S. Zhang, J. Yu, A. Zhang, F. Zhang, Spiraling motion of underwater gliders: Modeling, analysis, and experimental results, Ocean Eng. 60 (2013) 1–13. https://doi.org/10.1016/j.oceaneng.2012.12.023.

[26] R. Benzi, S. Ciliberto, R. Tripiccione, C. Baudet, F. Massaioli, S. Succi, Extended self-similarity in turbulent flows, Phys. Rev. E 48 (1993) R29–R32. https://doi.org/10.1103/PhysRevE.48.R29.

[27] J. Theiler, S. Eubank, A. Longtin, B. Galdrikian, J. D. Farmer, Testing for nonlinearity in time series: the method of surrogate data, Physica D 58 (1992) 77–94. https://doi.org/10.1016/0167-2789(92)90102-S.

[28] T. Schreiber, A. Schmitz, Surrogate time series, Physica D 142 (2000) 346–382. https://doi.org/10.1016/S0167-2789(00)00043-9.

[29] Z.-S. She, E. Lévêque, Universal scaling laws in fully developed turbulence, Phys. Rev. Lett. 72 (1994) 336–339. https://doi.org/10.1103/PhysRevLett.72.336.

[30] E. P. Chassignet, H. E. Hurlburt, O. M. Smedstad, G. R. Halliwell, P. J. Hogan, A. J. Wallcraft, R. Baraille, R. Bleck, The HYCOM (HYbrid Coordinate Ocean Model) data assimilative system, J. Mar. Syst. 65 (2007) 60–83. https://doi.org/10.1016/j.jmarsys.2005.09.016.

[31] J.-M. Lellouche, E. Greiner, R. Bourdallé-Badie, G. Garric, A. Melet, M. Drévillon, C. Bricaud, M. Hamon, O. Le Galloudec, C. Regnier, et al., The Copernicus global 1/12° oceanic and sea ice GLORYS12 reanalysis, Front. Earth Sci. 9 (2021) 698876. https://doi.org/10.3389/feart.2021.698876.

[32] L. Merckelbach, D. Smeed, G. Griffiths, Vertical water velocities from underwater gliders, J. Atmos. Ocean. Technol. 27 (2010) 547–563. https://doi.org/10.1175/2009JTECHO710.1.

[33] F.-X. Le Dimet, O. Talagrand, Variational algorithms for analysis and assimilation of meteorological observations: theoretical aspects, Tellus A 38 (1986) 97–110. https://doi.org/10.1111/j.1600-0870.1986.tb00459.x.

[34] P. Courtier, J.-N. Thépaut, A. Hollingsworth, A strategy for operational implementation of 4D-Var, using an incremental approach, Q. J. R. Meteorol. Soc. 120 (1994) 1367–1387. https://doi.org/10.1002/qj.49712051912.